Master's Thesis

Micro-sized Aluminum-air battery based on single-crystal Metal-organic frameworks as air cathode

EunYoung Cho

Department of Chemistry

Graduate School of UNIST

2017

Micro-sized Aluminum-air battery based on single-crystal Metal-organic frameworks as air cathode

EunYoung Cho
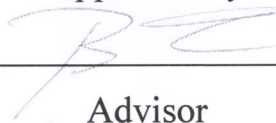
Department of Chemistry

Graduate School of UNIST

Micro-sized Aluminum-air battery based on single-crystal Metal-organic frameworks as air cathode

A thesis/dissertation
submitted to the Graduate School of UNIST
in partial fulfillment of the
requirements for the degree of
Master of Science

EunYoung Cho

11/23/2016 of submission

Approved by

_____

Advisor

Bartosz A. Grzybowski

Aluminum-air battery based on single-crystal

Metal-organic frameworks as air cathode

EunYoung Cho

This certifies that the thesis/dissertation of EunYoung Cho is approved.

11/23/2016 of submission

signature

_____

Advisor: Bartosz A. Grzybowski

signature

_____

typed name: Kwang S. Kim

signature

_____

typed name: Seok Min Yoon

signature

_____

Abstract

Aluminum-air batteries are promising energy sources due to their high theoretical voltage (2.7 V), high theoretical energy density (8.1 kWh/kg-Al), low cost, and safety and environmental friendliness etc.[1,2,3,4] However Al self-corrosion is limitation in Al-air battery− in aqueous alkaline electrolytes, causing formation of passivating $Al(OH)_3$ layer from $Al(OH)_4^-$ – is a major obstacle preventing continuous electrochemical reaction during discharge. Moreover, direct contact between Al and water (H_2O) results in parasitic hydrogen evolution reaction which, in turn, lowers the operating potential of the battery. Here, we, achieve inhibition of parasitic corrosion by using (i) a polyester anion transport layer with Zn particles embedded in it[5,6,7] and, most importantly, (ii) a single crystal of rubidium-cyclodextrin-metal-organic framework (Rb-CD-MOF) which not only serves as an air-cathode reducing oxygen but also as a diffuser[8,9] for $Al(OH)_4^-$ and OH^- ions to minimize the formation of $Al(OH)_3$ passivation layer on the anode. Furthermore, the Rb-CD-MOF itself exhibits bifunctional electro-catalytic effect [10,11] by supporting efficient and stable oxygen reduction reaction (ORR) close to the direct four-electron process, and also oxygen evolution reaction (OER). This ORR/OER bifunctionality allows the battery to efficiently use humid air (i.e., oxygen and water) as "fuel" powering its operation. Because of the inhibition of Al corrosion and the MOF's bifunctional electro-catalysis, the Al-air battery shows ultra-high discharge capacity. above 15,000 mAh/cm^2. The use of single-crystal electrocatalytic MOFs is a novel concept in battery design and, as illustrated by this work, can enhance performance of traditional batteries often limited by interfacial processes.

Contents

List of Figures

List of Tables

Chapter I. General Introduction

1.1 Introduction

1.1.1 Electrochemical energy storage system

The demands of sustainable energy have been increased continuously due to limitation of fossil fuel. Moreover, emission of CO_2 during combustion of the fossil fuels cause environmental pollution. Therefore, the researches of renewable energy such as solar, wind and tidal etc are rising. Among energy conversion systems, electrochemical conversion systems are popular owing to possibility to have high energy and power density for electrical vehicles and portable devices including mobile phone, note book etc. Batteries, fuel cells and supercapacitor are representative electrochemical systems.

Batteries are widely used in for example autonomous, portable, micro heat power and automotive (ex.Tesla motors- model s) (Figure 1.1).
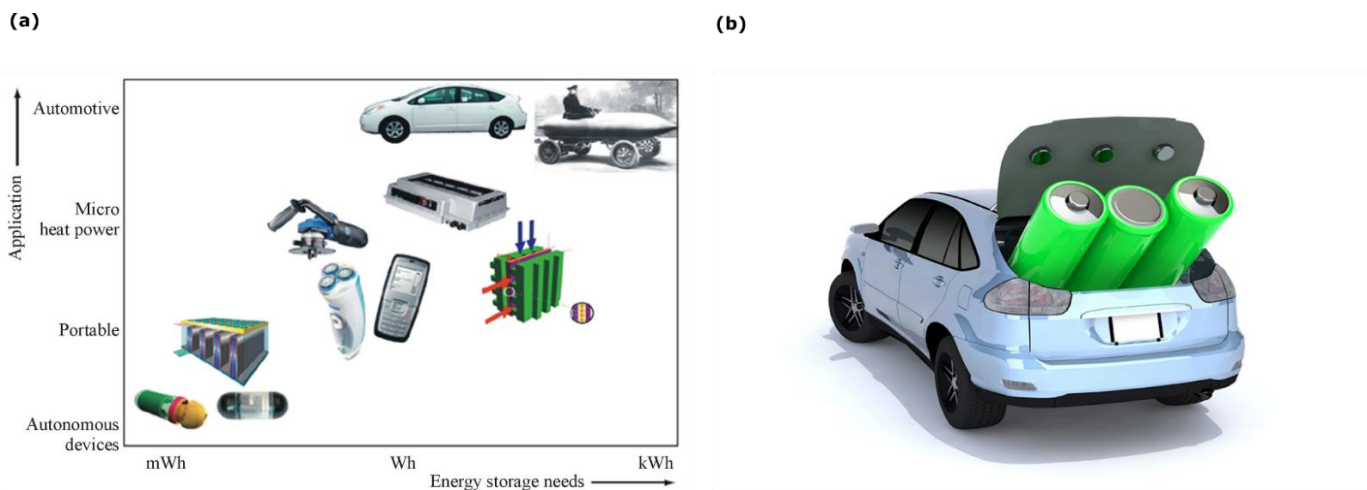
Figure 1.1 (a) various batteries applications of industry and (b) electrical vehicles.

The EVs are required to high energy, high power, small weight and safety. Several batteries were utilized to EVs that include lead-acid,NiCd,nickel metal hydride, Li-ion, Li-ion polymer, and, less commonly, zinc-air and molten salt batteries. These batteries are explained in next part.

Basic conceptual models of batteries are Galvanic cell and Daniel cell (Figure 1.2).

(a)

Zinc anode   Copper cathode

$Zn_{(s)}$ Porous disk $Cu_{(s)}$

Anion flow

$Zn^{+2}_{(aq)}$ $Cu^{+2}_{(aq)}$

$ZnSO_4$ (aq) $CuSO_4$ (aq)

(b)

electrons

salt bridge

zinc ions   sulfate ions

zinc electrode   copper electrode

zinc sulfate   (−) anode oxidation   (+) cathode reduction   copper (II) sulfate
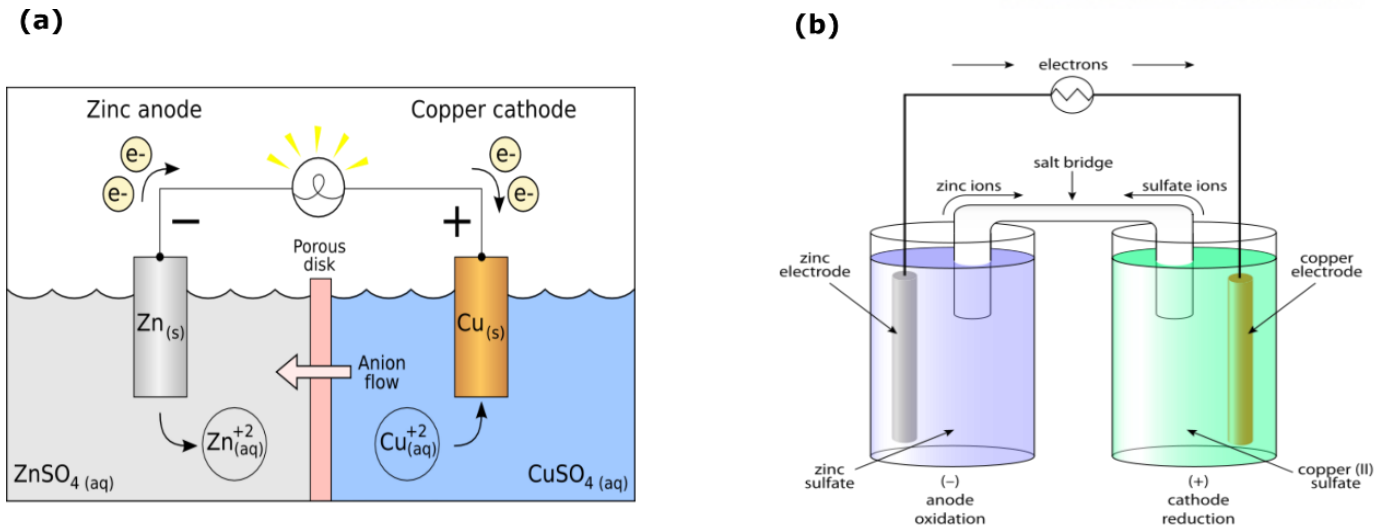
Figure 1.2 Schematic illustrations of (a) Galvanic cell (b) Daniel cell.

In the Galvanic cell, redox reaction is happened at interface of electrodes and electrolyte. The metal is oxidized to cation at anode, the electron is transferred to cathode. The Galvanic cell is unable to operate long time because ions are attached electrode then, electrode are blocked that interrupt electron transfer. However, Daniel cell has salt bridge which protects to polarization by moving cations and anions for charge balance. The batteries are close system that means batteries are operated by reaction of ions in electrolyte. On the other hands, fuel cells are open system in electrochemical energy systems. Fuel cells can be supplied fuels from outside constantly from external source (ex. oxygen, hydrogen, alcohol etc as fuels). Fuel cells cannot electrical recharge, but after use, the fuels are supplied thus, fuel cell have high energy density (Figure 1.3).

(a)

e^-

Anode   Cathode

Separator
Electrolyte

Battery

(b)

e^-

Anode $4OH^-$ Cathode

$4H^+$

$2H_2O$

$2H_2$ O_2

Separator
Electrolyte
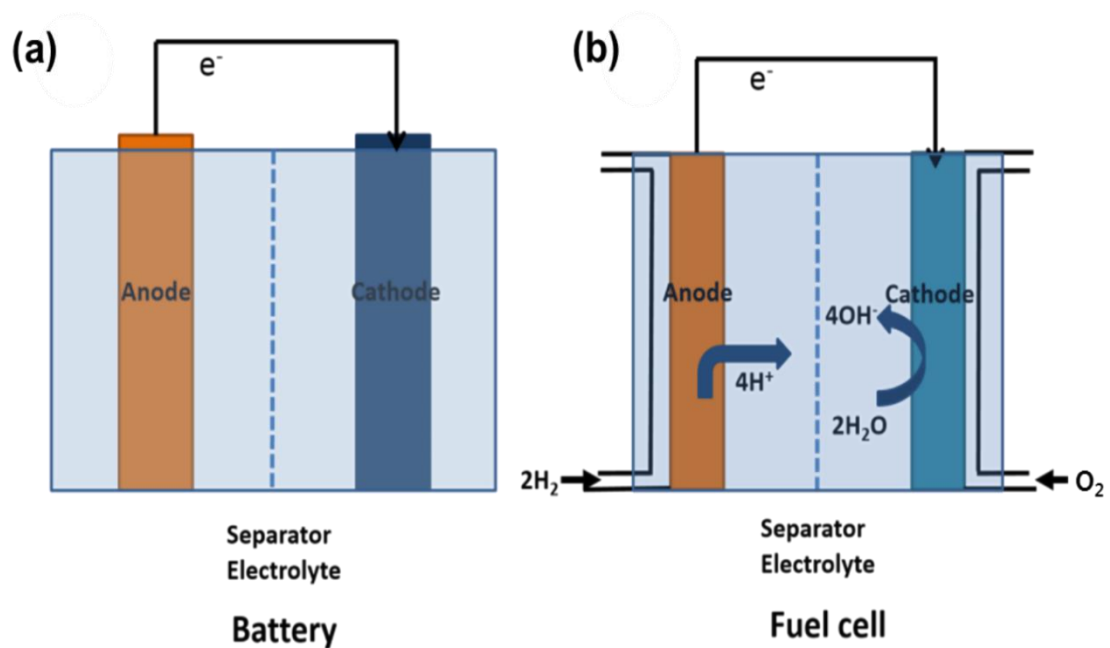
Fuel cell

Figure 1.3. Simplified scheme of (a) battery and (b) fuel cell.

In the electrochemical energy systems, cell voltage, specific energy, specific power and specific capacity are significant factors for evaluating performance of the systems.

In order to determine working voltage of batteries and fuel cells, thermodynamics is important. When a process is carried out at constant temperature and pressure, maximum work is equal to change in free energy:

$$w_{max} = \Delta G$$

For electrochemical cell,

$$w_{max} = -qE_{max} = \Delta G \ (q = nF)$$

q is charge, E is cell potential, n is number of electron and F is Faraday constant.

$$\Delta G = -qE_{max} = -nFE_{max}$$

For standard condition

$$\Delta G^o = -nFE^o$$

And from this process,

$$\Delta G = \Delta G^o + RT \ln (Q) = -nFE = -nFE^o + RT \ln (Q)$$

Q is Reaction quotient - The mathematical product of the concentrations of the products of the reaction divided by the mathematical product of the concentrations of the reactants. R is gas constant T is absolute temperature.

$$E_{cell} = E_{cell}^o - RT/nF \ \ln(Q)$$

This Nernst equation which gives evidence to get cell potentials.

Specific energy (Wh/kg), energy density (Wh/L) are energy contents and specific power (W/kg), power density (W/L) are power contents. The electrochemical systems are classified depends on these factors. Following these factors, the electrochemical energy systems are displayed in ragone diagram (Figure 1.4).
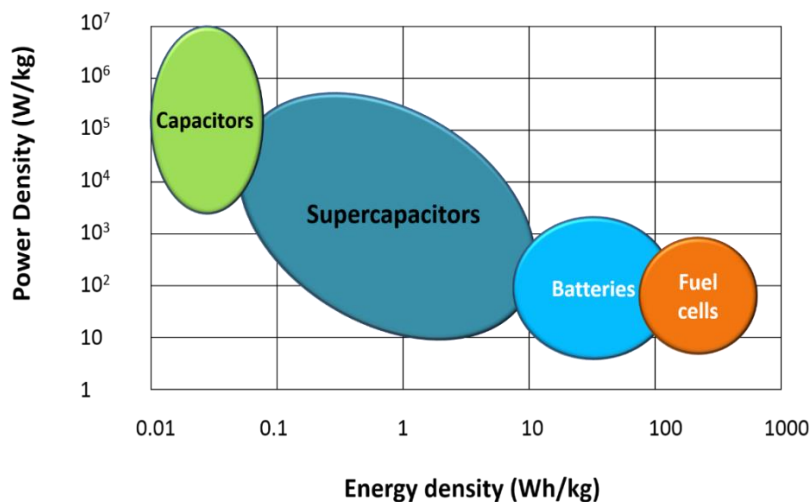
Figure 1.4. Ragone diagram for comparison of electrochemical energy conversion and storage systems

4

As the diagram has shown that capacitors have high power, fuel cells have high energy and batteries are intermediate of them. Supercapacitors are one of electrochemical energy system that is usually used to describe an energy storage system based on electrical double layer (EDL) with high surface of carbon. When an electrode that is, electrical conductor, is immersed into electrolyte, there is spontaneous organization of charges at surfaces of electrode and electrolyte is facing the electrode. This EDL is formed and released, which results parallel movement of electrons. The supercapacitors are capable of store energy and release the energy in a short time. but here, supercapacitors are not considered.

lately, people have studied to improve electrochemical systems to make hybrid devices such as capacitor-batteries, batteries-fuel cells.

In particular, fuel cells have high energy density but, lower power density than batteries due to slow kinetics of cathode side. For such reason metal-air batteries are studied to supplement disadvantages of batteries and fuel cells. Therefore, metal-air batteries are covered here.

1.1.2 History of batteries markets

In the batteries markets, a graphical representation of energy capabilities is shown in figure 1.5. Various batteries such as lead-acid, zinc/halogen, metal-air, sodium-beta, nickel metal hybrid, and lithium-ion have been used. Typically, the issues of batteries are not only batteries performance but weight, cost and safety. The batteries have developed toward satisfied these factors.
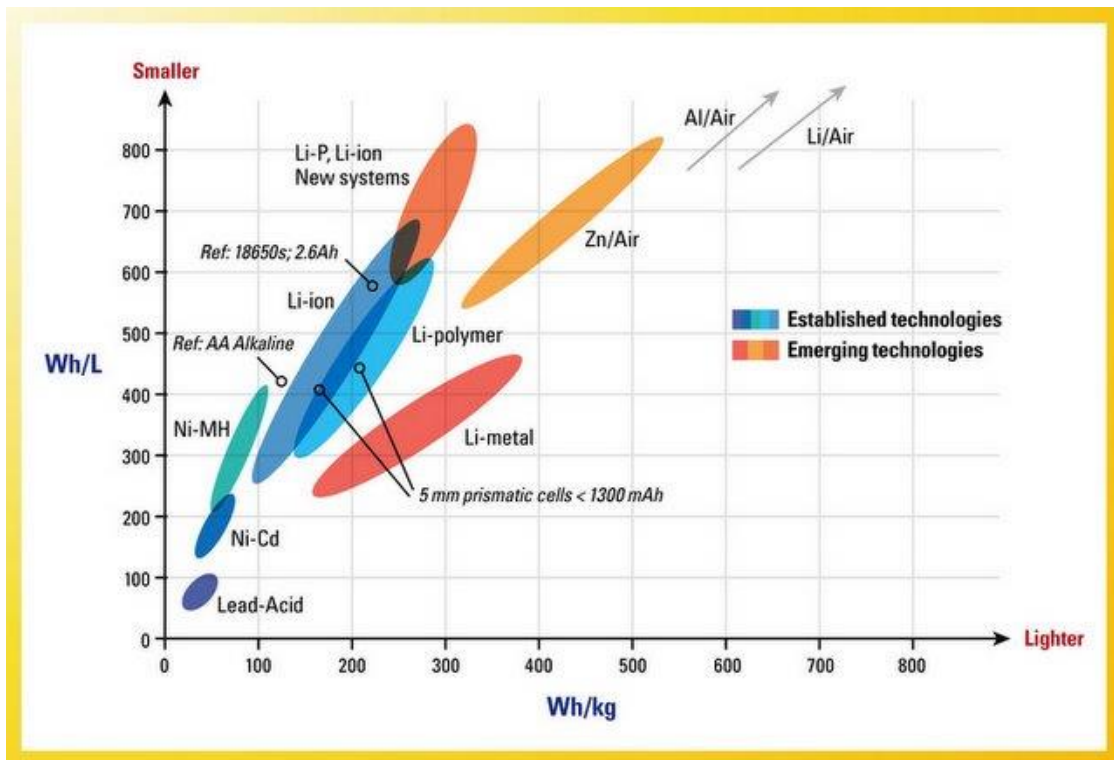
Figure 1.5. Energy storage capabilities of common commercial batteries.

Lead-acid batteries were oldest type of batteries that could be used to EVs due to improving of cycle-life, promising cost, and specific power[15]. However, the limiting factors of lead-acid batteries are relatively low cycle life and battery operational lifetime. The cycle life of lead-acid batteries is damaged by discharge and temperature[16].

NiMH batteries is rapidly emerged to substitute lead-acid batteries. NiMH batteries were correspondingly specific power and lifetime. However, NiMH batteries, which are limited expansion due to disadvantages of large size and heavy weight[17].

Li-ion batteries were replacement of NiMH batteries due to theirs high cell voltage, low self-discharge, high energy density and lighter weight. Li-ion batteries are currently favorite a mobile applications and EVs. However, Li-ion batteries are disadvantages such as high cost, low temperature tolerance, and need for protective circuity to prevent cell degradation and thermal runaway. Moreover, even if Li-ion batteries have high energy density which are less than gasoline. The Li-polymer batteries are made of same model with Li-ion batteries, only electrolyte is changed to solid polymer that provide safety and flexible cell design. However, the cost is increased and scale is larger.

Above diagram, the metal-air batteries are expressed emerging technologies that means these studies are insufficient. Metal-air batteries are located in position where is the smaller size and lighter weight. Thus metal-air batteries have potential to make commercial batteries. For example, EVs are required to high energy density, high power density that means batteries inside of EVs are small and light. For such reason, currently, researches of metal-air batteries are glowing.

1.2 Metal-air batteries

Metal-air batteries are emerged from combination of batteries and fuel cells schemes to improve performance. Metal-air batteries consist of pure metal as an anode, and external cathode of ambient air with electrolyte. Metal-air batteries are attractive electrochemical energy system since the batteries are capable of using oxygen from air as reactant consistently[18]. Therefore, metal-air batteries can have high energy density (Figure 1.6)
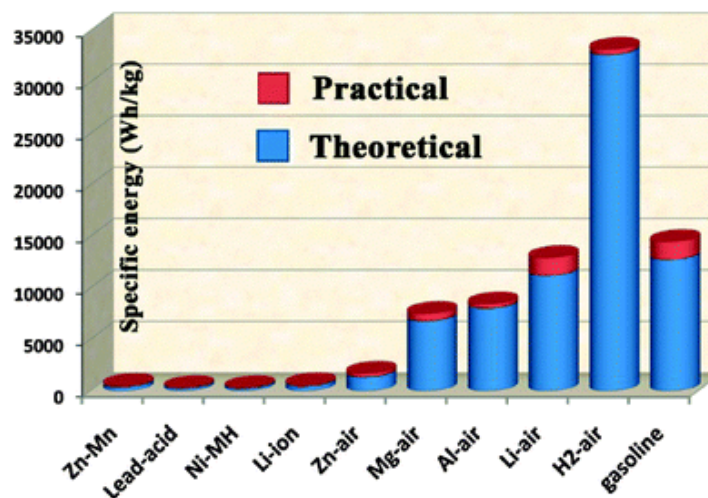
Figure 1.6 Comparison of energy density in various batteries.[19]

In addition, metal-air batteries have potentials of cheap price and reducing weight of the battery because the cathode is oxygen from air. Consequently, many researchers have concentrated on this system but, this studies are still in-process.

1.2.1 Anode of metal-air batteries.

Metal-air batteries are used pure metal as an anode such as Li, Zn, Al and Mg etc. Among the metals as anode, Li and Zn are representative metals for metal-air batteries (Figure 1.7).

Li-air batteries have ten times higher energy density than Li-ion batteries. However, Li-air batteries have many challenges which are incomplete porous carbon cathode blocking, unstable anode in vapor and lack of catalysts effect at cathode etc. Thus, Li-air batteries cannot have applied industry. Li-air batteries are divided two types depends on electrolytes: aprotic electrolyte and aqueous electrolyte. The Li-air batteries chemical reactions at each of aprotic and aqueous electrolytes are shown below.
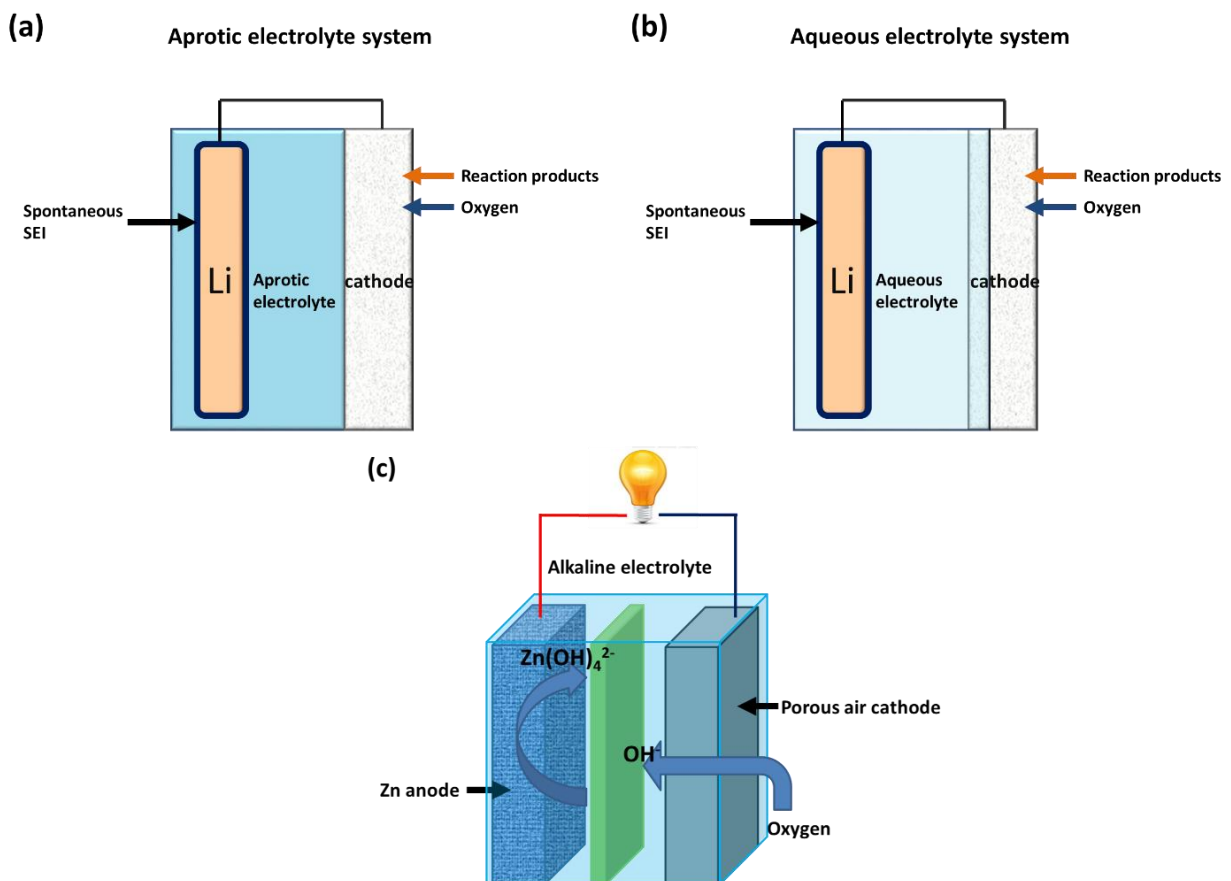
Figure 1.7. Representative metal-air batteries (a) aprotic electrolyte and (b) aqueous electrolyte Li-air batteries (c) Zn-air batteries.

In the cell with an aprotic electrolyte, lithium oxides are produced at the cathode:

$$Li^+ + e^- + O_2 \rightarrow LiO_2$$
$$Li^+ + e^- + LiO_2 \rightarrow Li_2O_2$$
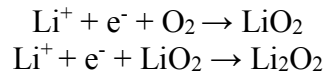
Lithium oxides are insoluble in aprotic electrolytes, which leads to cathode clogging[20].
In a cell with an aqueous electrolyte, lithium hydroxide is produced at cathode:

$$\text{Acidic electrolyte: } 2Li + 1/2\ O_2 + 2H^+ \rightarrow 2Li^+ + H_2O$$
$$\text{Alkaline aqueous electrolyte: } 2Li + 1/2\ O_2 + H_2O \rightarrow 2LiOH$$
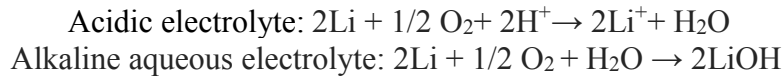
Typically, Li metal react with moisture violently thus, there are many attempts for finding appropriate electrolytes. Even though the efforts for demonstration of Li-air batteries including to combine aprotic and aqueous electrolytes are continuing, water explosively is still hazard to employ Li-air batteries in industry.

Zn-air batteries have theoretical energy density of 1086 Wh/kg about five times higher than lithium ion cells[25]. Zn-air battery is comprised of zinc metal as anode, oxygen as cathode and a membrane separator in alkaline electrolyte. The oxygen from ambient air flowed into the gas diffusion electrode. The oxygen reduction reaction (ORR) to hydroxyl ion is occurred at the air cathode and electrons are generated through metal anode reaction and hydroxyl ion is moved to metal anode. Overall electrochemical reaction is shown below.

$$\text{Anode: } Zn \rightarrow Zn^{2+} + 2e^-$$
$$Zn^{2+} + 4OH^- \rightarrow Zn(OH)_4^{2-},$$
$$Zn(OH)_4^{2-} \rightarrow ZnO + H_2O + 2OH^-, E_o = 1.25\ V.$$

$$\text{Cathode: } O_2 + 2H_2O + 4e^- \rightarrow 4OH^-, E_o = 0.4\ V.$$

$$\text{Overall reaction: } 2Zn + O_2 \rightarrow 2ZnO, E_{overall} = 1.65\ V.$$

$$\text{Parasitic reaction: } Zn + 2H_2O \rightarrow Zn(OH)_2 + H_2$$
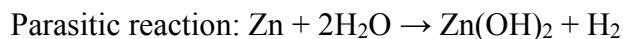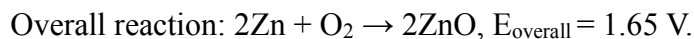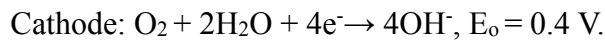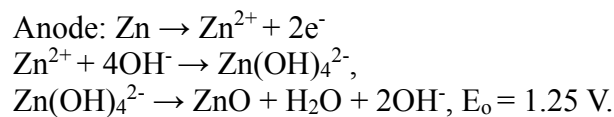
Al-air batteries are one of metal-air batteries which have high energy density. Al metal is attractive candidate to metal-air batteries due to low cost, environmental friendless, abundance of earth. Al-air batteries are made of Al metal as anode, porous carbons as cathode and electrolyte (Figure 1.8).
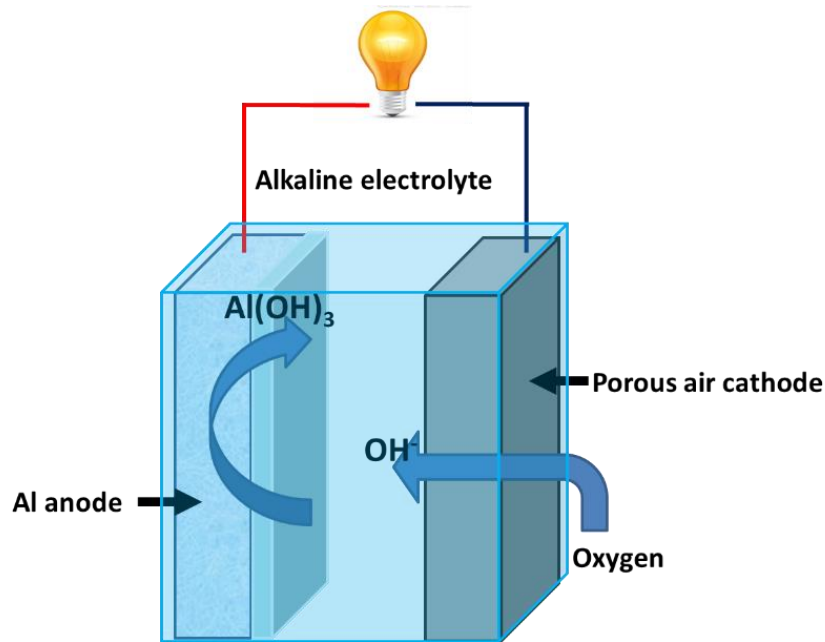
Figure 1.8. Scheme of Al-air batteries.

The Al-air batteries are occurred following this redox reaction:

Anode: Al$\rightarrow$ Al^{3+}+3e-
Al+3OH$^-\rightarrow$ Al(OH)$_3$, E$_o$= -2.31V

Cathode: O$_2$+2H$_2$O+4e$^-\rightarrow$ 4OH$^-$, E$_o$= 0.40V

Overall reaction: 4Al+3O$_2$+6H$_2$O$^-\rightarrow$ 4Al(OH)$_3$, E$_{overall}$= -2.7 V

Parasitic reaction: Al+3H$_2$O $\rightarrow$ Al(OH)$_3$+ 3/2H$_2$
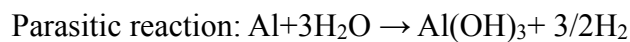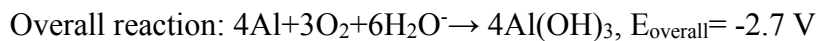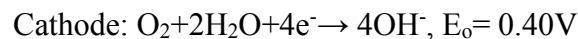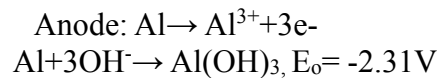
Al-air battery has matter of self-corrosion that is major obstacle in making commercial scale. The oxidation is occurred on Al surface that hinder further battery process by forming Al to Al$_2$O$_3$ and Al(OH)$_3$ passivation layer. Moreover, parasitic hydrogen evolution reaction drops potential of batteries. For such reason, some people used Al alloy such as Al-Zn, Al-In, Al-Ga and Al-Sn[21,22,23,24]as replacements of pure Al. In particular, the alloy of In, Zn and Al protects corrosion since Zn has proven to reduce hydrogen evolution by increasing hydrogen evolution potential. (cathodic protection). Typically, Al-air batteries are non-rechargeable due to stop generating electricity from formation of aluminum oxide layer. Therefore, many studies have made cathode material which has bifunctional electocatalytic effect to develop cell performance and fabricate rechargeable batteries. Next part, electrocatalysis materials as cathode are covered.

1.2.2 Air cathode

The air cathode is one of key components in metal-air batteries. Even though metal-air batteries have high theoretical energy density, practical energy density is demonstrated depends on cathode materials. In metal-air batteries or fuel cells, oxygen reduction reaction(ORR) and oxygen evolution reaction(OER) are most important reactions. Oxygen reduction reaction is that oxygen is reduced to hydroxide by electron from metal and combined with metal ion during discharge[25]. ORR chemical reaction is different depending on electrolyte:

$$\text{ORR, alkaline solution: } O_2 + 2H_2O + 4e- \rightarrow 4OH^-, E_o = 0.40 \text{ V}$$
$$\text{acid solution: } O_2 + 4H^+ + 4e^- \rightarrow 2H_2O, \quad E_o = 1.229 \text{ V}$$
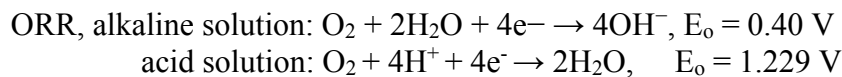
ORR has two pathways from moving number of electron. One is $4e^-$ process which is oxygen directly reduced to H_2O and another is $2e^-$ process from oxygen to H_2O_2.

Typically, oxygen kinetics is very sluggish. Thus cathode materials are required large surface area to make fast ORR kinetics. Many studies have found materials to speed up ORR kinetics such as Pt, Ru and Ir. [26,27] Although these materials have shown better ORR performance, high cost is matter in applying as commercial cathode materials.

Thus, several alternative materials such as nanocarbons[28,29], metal oxides[30,31], carbide or nitrides and their composite[32,33,34,35].have been discovered as electrocatalysts however, the carbon materials still have less activities than Pt/C[36].

In general, ORR is preferred occurring potential which is closer reversible electrode potential and ORR occurs potential under reversible electrode potential. If anodic current equal to cathodic current, external current is zero in reversible reaction. That is exchange current(i_o):

$$i_o: nFk_a \text{ [R] exp } (\alpha_a nFE_{eq}/RT) \text{ or } nFk_c \text{ [O] exp } (-\alpha_c nFE_{eq}/RT)$$

n is number of electron transferred, F is faraday constant, k_a and k_c are rate constant, α is transfer coefficient, [O] and [R] are internal concentration of reactants, R is gas constant and T is absolute temperature. The exchange current density is described by reaction and on the electrode surface where is happened chemical reactions.

The overpotential is $\eta = E - E_{eq}$, E is practical potential.
Butler-Volmer equation gives information about relationship current and overpotential:

$$i_c = nFk_c \text{ [O] exp } (-\alpha_c nF(E-E_{eq})/RT) \text{ exp } (-\alpha_c nFE_{eq}/RT)$$
$$= i_o \text{ exp } (-\alpha_c nF\eta/RT)$$

In this equation, to obtain high current density, low overpotential and large exchange current density are required.

The oxygen evolution reaction(OER) is one of important reactions in electrocatalysis. OER arise as different chemical reaction depending on electrolyte.

$$\text{OER, alkaline solution: } 4OH^- \rightarrow O_2 + 2H_2O + 4e^- \quad E_o = 0.40 \text{ V}$$
$$\text{acid solution: } 2H_2O \rightarrow O_2 + 4H^+ + 4e^- \quad E_o = 1.229 \text{ V}$$
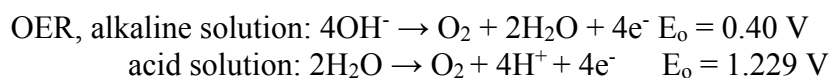
The OER is occurred at metal oxide as an anode which is made thin film by Pt, Au, Ir and Rh. Because oxide film is generated at potential area where oxygen evolves. To use anode materials in the OER, low overpotential and stability are essential. For example, RuO_2 and IrO_2 have good performance of OER, IrO_2 needs be stabilized by thermal treatment. Ni is used widely for OER, but $Ni4^+$ which is low conductivity and high potential formed during the reaction that read to drop OER performance.[37]

The OER reaction pathway is complex and mechanisms are changed by electrode. Many intermediate states are existed OER steps. The OER is induced from Tafel plot. The tafel equation is shown relation of electrochemical kinetics and the overpotential and also give evidence of number of electron transferred the reaction (Figure 1.9).
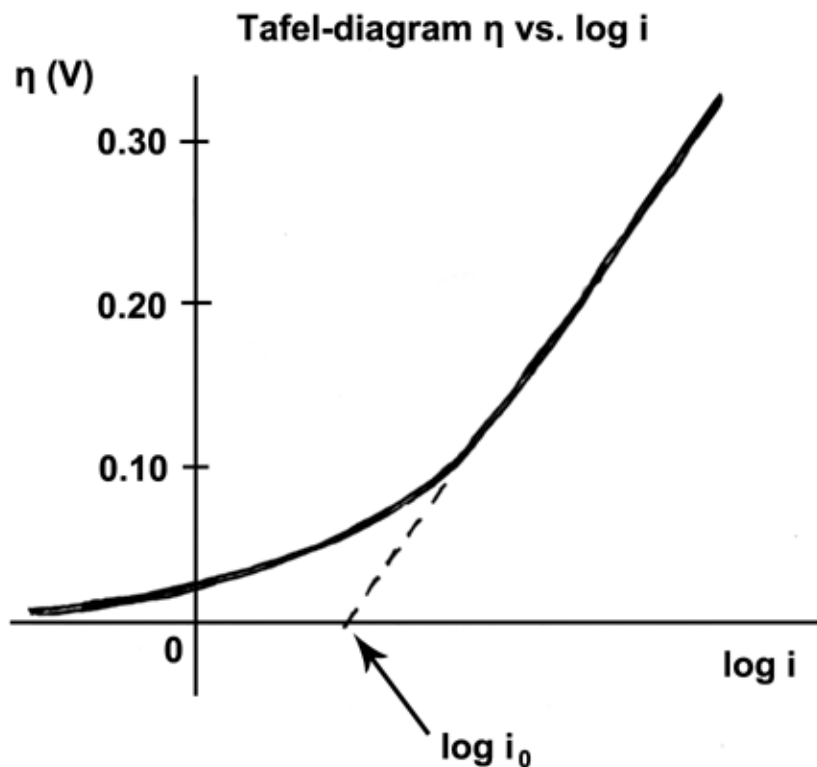
Figure 1.9. Tafel plot for anodic process.

$$\eta = A \times \ln(i/i_o)$$

η is overpotential, A is slope and i is current density and i_o is exchange current density.

$$\eta = a + b \log(i)$$

b is Tafel slop ($0.059/n\alpha$) n is electron transferred, α is transfer coefficient.

Rotating disk electrode (RDE) is used to analyze these ORR and OER. In the

electrolyte, when anions and cations are diffused, these ions have same rate of diffusion. but, one is faster than another, equilibrium is broken. To protect breaking of equilibrium, RDE measure reaction with less effect diffusion rate by electrode rotation. The rotation of electrode generates centrifugal power that lead ions move to electrode.

Another analyzer is rotating ring –disk electrode (RRDE) that is same model with RDE but additional ring is attached at electrode. RRDE have each of different potentials at ring disk and rotating disk. The reaction is occurred at rotating disk then, the products are moved to ring disk to react again. The products from rotating disk can be analyzed by this process.

1.3 Metal Organic Frameworks (MOFs)

Metal-organic frameworks (MOFs) are open metal framework with crystalline that are self-assembled by metal ions and organic linkers (Figure 1.10).[38,39,40,41] In 1990, Hoskins and Robson reported on the design of 3D metal-organic frameworks using Cu(I) metal and organic linker[42,43]. After that, Moore[44], Yaghi[45] and Zaworotko[46] offered possibilities of new structures and properties by publishing these coordination polymer. Particularly, bridging ligand react with metal ion which has vacant or labile site[47].Thus Metal-organic frameworks(MOFs) have large pore and large surface area. (Figure 1.11). Many studies of MOFs are using this large surface area to various applications.
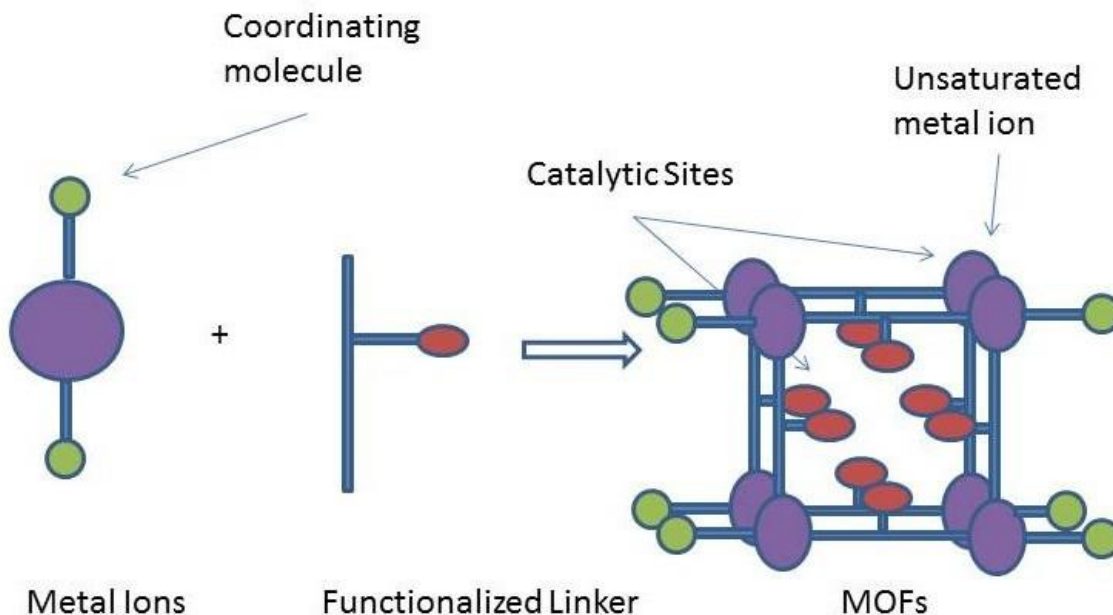
Figure 1.10. Mechanism of Metal-organic frameworks.
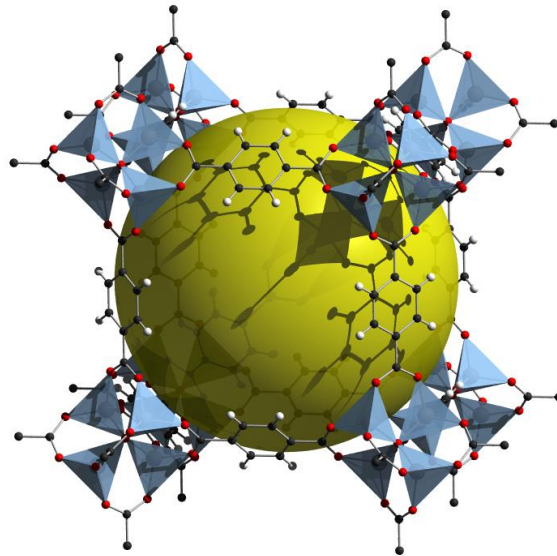
Figure 1.11. The Metal-organic framework with large pore (MOF-5).

One of the issues in MOFs area was to design a stable framework. Inside of MOF pores, it has guest molecules from solvents or template. However, the attempts to remove guest molecules from pore were often failed due to collapse of framework. Therefore, rigidity and stability of MOF are significant factors. Yaghi and coworkers reported the synthesis of a MOF which remains crystalline and stable secondary building blocks (SBUs)[48,49,50]. The clusters of carboxylate are mulidentate linkers allow for the formation of more rigid frameworks since that can be aggregated with metal ions into M-O-C bridges[39]. MOFs are promising material for many applications in catalyst[51,52], gas storage[53,54,55,56], separation and molecular recognition[57] due to their properties inherent to the building block such as geometry rigidity chemical functionality, or chirality. Particularly, storage applications such as gas, chemicals, toxic materials are studied. Furthermore, although people are interested in electrochemical energy storage applying MOFs[58,59,60], this experiments were not insufficient. But successive researches dealing with this subject and proved possibilities of MOF applications for electrochemical energy storage[61,62,63].

1.2.2 Examples of Metal-Organic Frameworks batteries applications

MOFs have large pore and large surface area. Thus, many applications using MOFs have studied including electrochemical applications. Particularly, MOFs are utilized to electrochemical systems. Electrochemical energy systems are considered in previous part. The MOF play role as electrode, electrolyte, catalysts and separator etc. For examples, some MOFs are used as electrode for Li-ion batteries[64,69,65,66], Na-ion batteries[67,68] and supercapacitors[69]. However, most of applications cannot be used pristine MOFs because MOFs are insulator. Thus, people have made carbon with high surface area from MOFs or metal oxide(MO) using MOFs as template. One of example is carbon from MOFs have shown electrocatalyst performance

(OER, ORR)[70,71]. Metal oxide(MO) is applied to batteries and supercapacitors.

In particular, MOFs are used to Li-S batteries as separator. Sulfur is good material as a cathode for Li-ion batteries. Li-S batteries give high specific capacity and energy density. However, sulfur has poor reversibility due to loss of active site during cycles[72] because MOF can obtain soluble polysulfide which can be dissociation during batteries cycle, inducing capacity decay and low efficient battery performance. However, MOF is capable of using as a separator since MOFs are porous materials. Zhou *et al.*[73] are reported Li-S batteries with MOFs separators enhanced battery cycle and structural stability.(Fig 1.12).
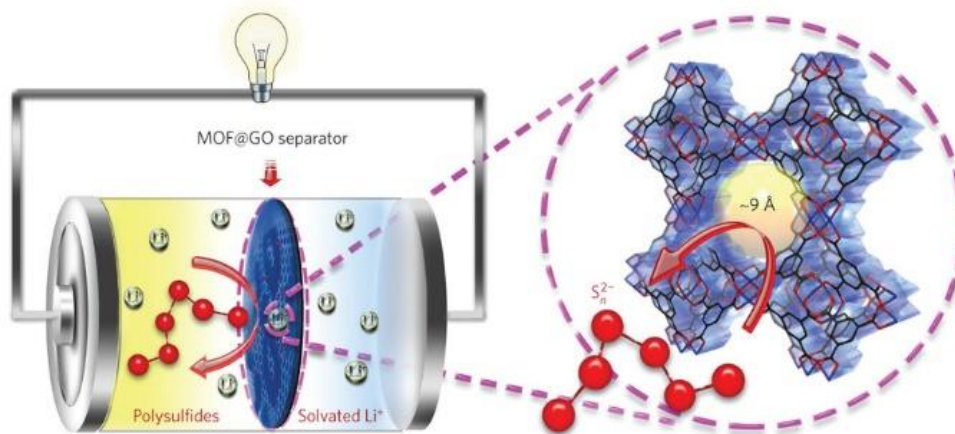
Figure 1.12. Example of Li-S battery with MOFs separator[95].

As the mention previously, pristine MOFs have not described as an electrode. Nevertheless, Long *et al.*, proved construction of dual ion prototype batteries using Fe_2 (dobpdc) MOF as cathode which is shown topotactic oxidative insertion reaction with weak coordinated anions including BF^- and PF^{-}[74] (Figure 1.13).
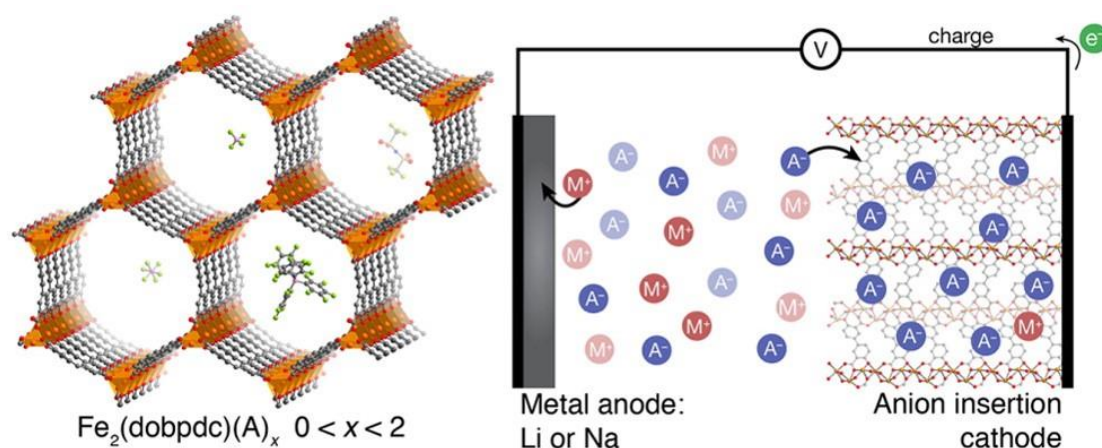
Figure 1.13. Example for MOFs as anode in batteries application[71]. A$^-$ is weekly coordination anions, M$^+$ is metal cations[97].

In general, MOFs are included in porous coordination polymers (PCPs) extensively. Several of PCPs and MOFs have been found high proton conductivity. However, there is no report on the application of solid electrolyte because proton carriers are leached from porosity. Therefore, to overcome this problem, kitagawa *et al.*[75] used defected nonporous coordination polymer as solid electrolyte for fuel cell (Figure 1.14). The defect site of coordination polymer crystal can encapsulate hydrogen carriers and improve hydrogen mobility that lead to high hydrogen conduction.
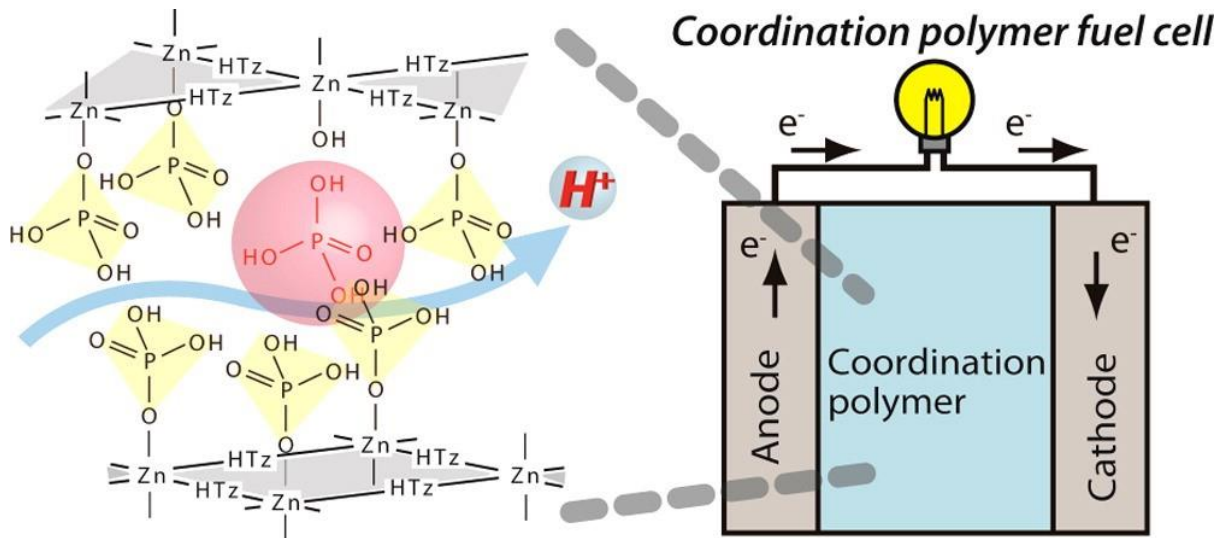
Figure 1.14. Example of solid electrolyte using coordination polymer crystals for fuel cell.

The above studies argued possibilities to applications for electrochemical energy system. MOFs can be electrode, electrolyte separator. In here, MOFs are considered to metal-air batteries system as air cathode.

Chapter II. Aluminum-MOF-air battery (AMA battery)

2.1 Introduction

The Al-MOF-air (henceforth, AMA) battery was assembled (i) by coating a polished Al foil (99.99 % Sigma Aldrich) with a ~10 μm think layer of polyester (Allied High-Tech Products) containing 0.02 w/w% of Zn nanoparticles (Sigma Aldrich, average diameter 40 nm, dispersity 0.16), (ii) placing onto this film a single-crystal, rubidium-based γ-cyclodextrin MOF(Figure 2.1) soaked with 1M RbOH (1M RbOH@Rb-CD-MOF), and (iii) covering the top surface of the MOF crystal with conductive carbon paste (Figure 2.2).
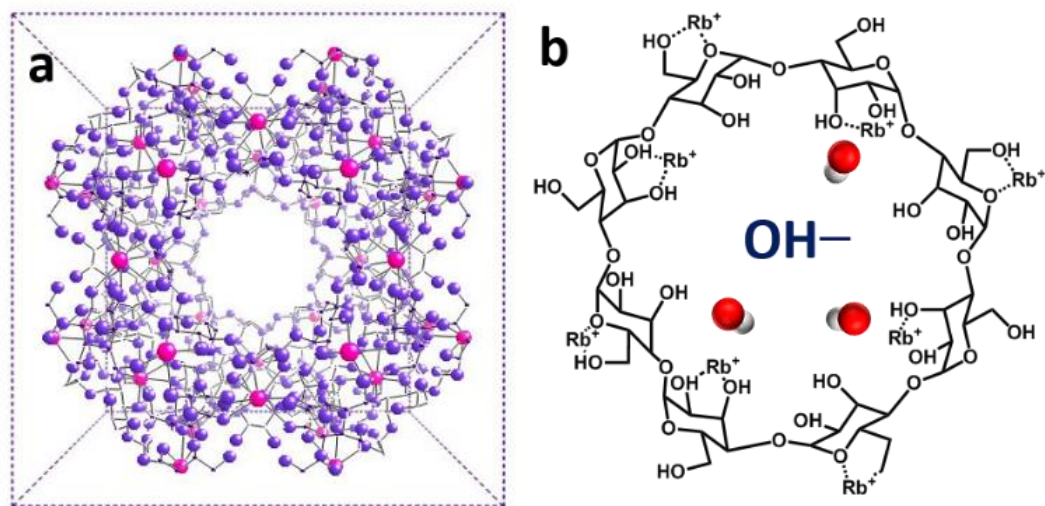
Figure 2.1. a) A unit cell of Rb-CD-MOF. **(b)** Coordination of Rb$^+$ cations to the γ-cyclodextrin (CD) scaffold and inclusion of OH$^-$ anions (just one is indicated for clarity) to balance MOF's net charge. Optical micrographs of Rb-CD-MOF crystals
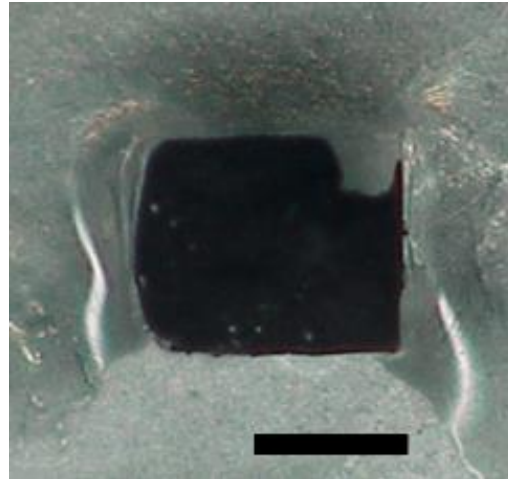
Figure 2.2. Image of MOF battery covering the top surface of the MOF crystal with conductive carbon paste.

The Rb-CD-MOF single crystals were synthesized as described before[76,77,78] and were typically ca. 200-600 m in each direction (with volumes on the order of 0.01~ 0.05 mm^3). These crystals harbored hydroxide anions (OH$^-$) balancing the charge of Rb$^+$ cations and enabling crystal's ionic conductivity measured by AC impedance to be 7.27 x 10^{-5} S/cm (Figure2.3).
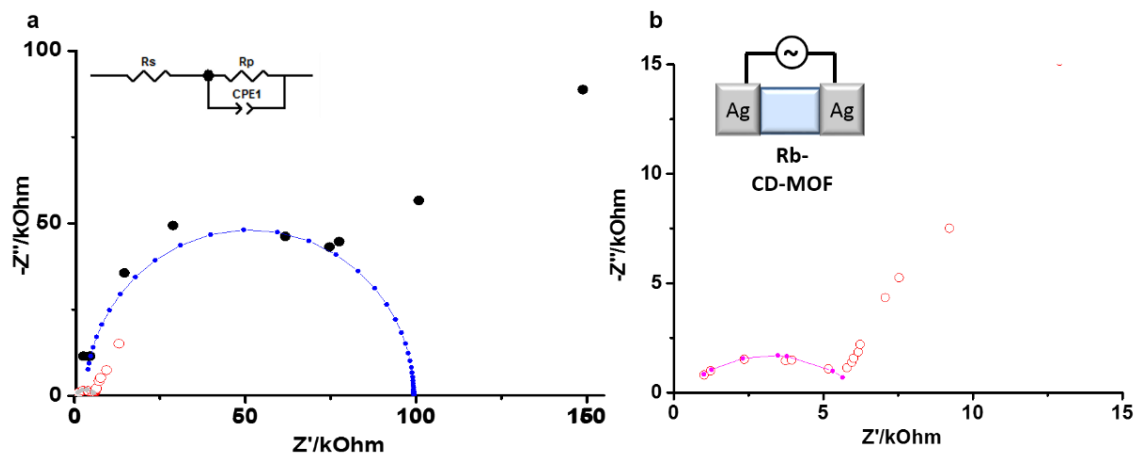
Figure 2.3. Impedance of Rb-CD-MOF to measure ion conductivity.

Moreover, this conductivity could be enhanced to 7.83 x 10^{-4} S/cm when the crystals were infiltrated with additional RbOH (by soaking in 1M RbOH solution of 70% MeOH and 30 % H$_2$O). Images in Figure 2.4 and the corresponding powder XRD spectra in Figure 2.5 confirm that the MOFs do not lose their crystallinity upon soaking, which agrees with our

previous reports.[78]

(a) **(b)**
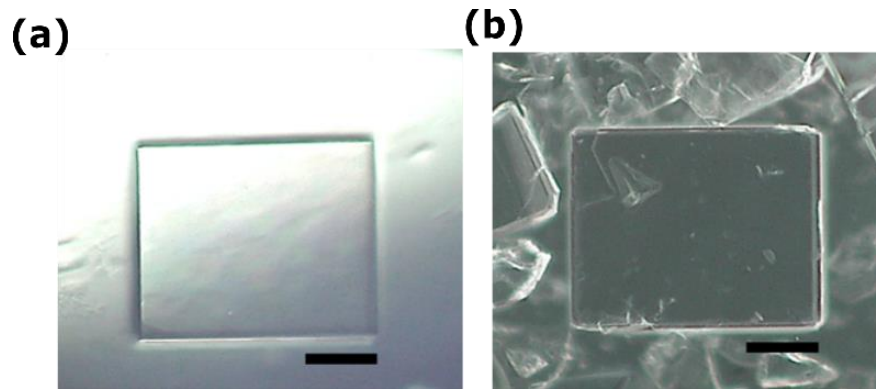
Figure 2.4. Optical micrographs of Rb-CD-MOF crystals (a) as-synthesized, and (b) infiltrated with 1M RbOH. Scale bars = 100 μm.
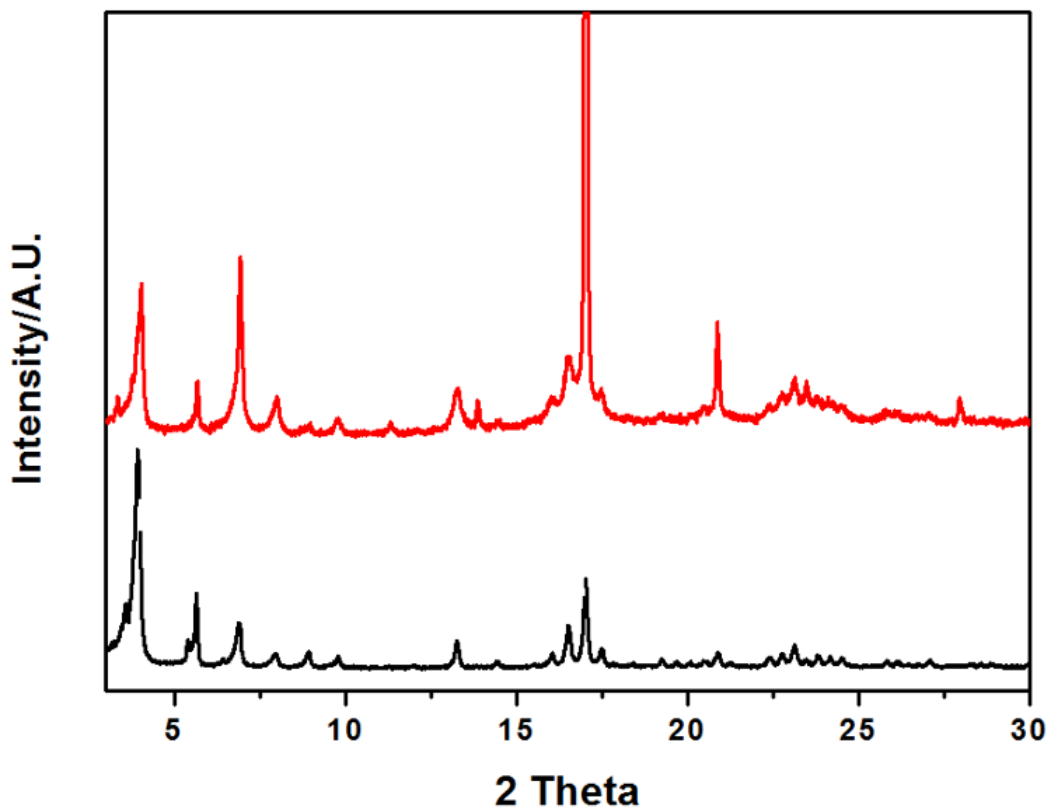
Figure 2.5. Powder x-ray spectra of RbOH@CD-MOF crystals as synthesized (black line) and infiltrated with 1M RbOH (red line).

We note that the above conductivity values are higher than for other ionically-conductive MOFs[79,80,81], likely on account of the hydrophilicity of channels and hydrogen bonding network between water and OH⁻ guests[81,82] Also, the ionic conductivity of the as-synthesized Rb-CD-MOF single crystals is one order of magnitude higher than that reported for polycrystalline CD-MOF pellets,[83] emphasizing the role of long-range ordering of MOF's channels and the lack of grain boundaries.[82]

2.2 Results

Figure 2.6 compares open circuit voltage (V_{OC}) of the AMA battery under humidified conditions with a conventional galvanic cell in which 1M KOH aqueous solution was used instead of the MOF monocrystal. While the former maintains V_{OC} at ca. 1.7 V for over 24 hrs, the latter exhibits rapid voltage drop.
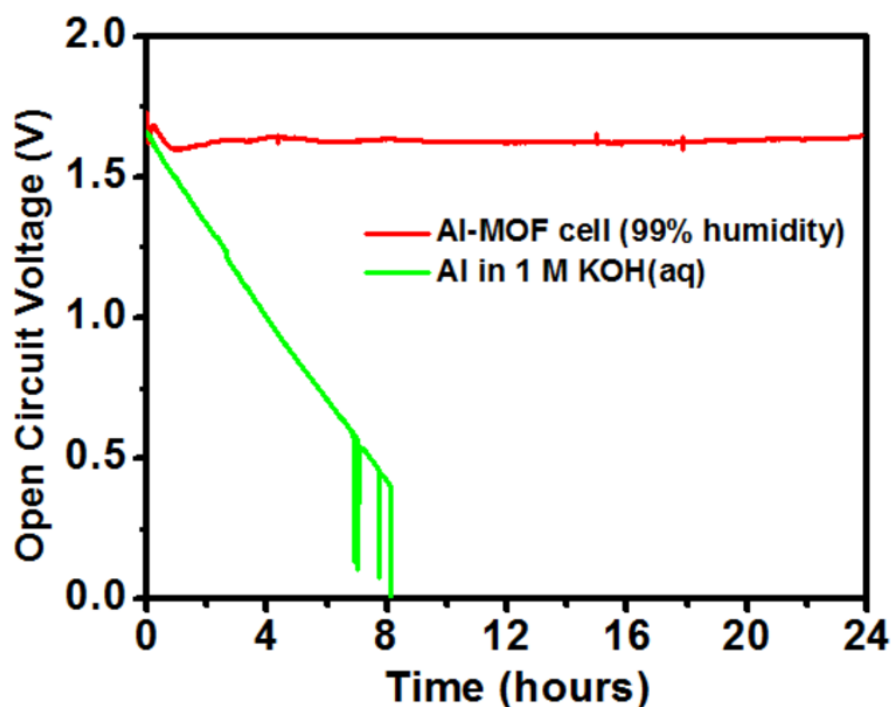
Figure 2.6. Red line plots the open circuit voltage of the AMA battery under humid conditions (99 % by bubbling dry air through a 3:7 v/v water/methanol mixture). The green line is for a galvanic cell comprising similar Al and glassy carbon electrodes but a 1M KOH solution instead of the electrolyte-infused Rb-CD-MOF crystal.

Figure 2.7 illustrates that the AMA battery under the same humidified atmosphere and discharge current as high as 100 mA/cm^2 maintains non-zero potential for over a week with specific capacity > 18,000 mAh/cm^2 and specific power > 11.7 Wh/cm^2).
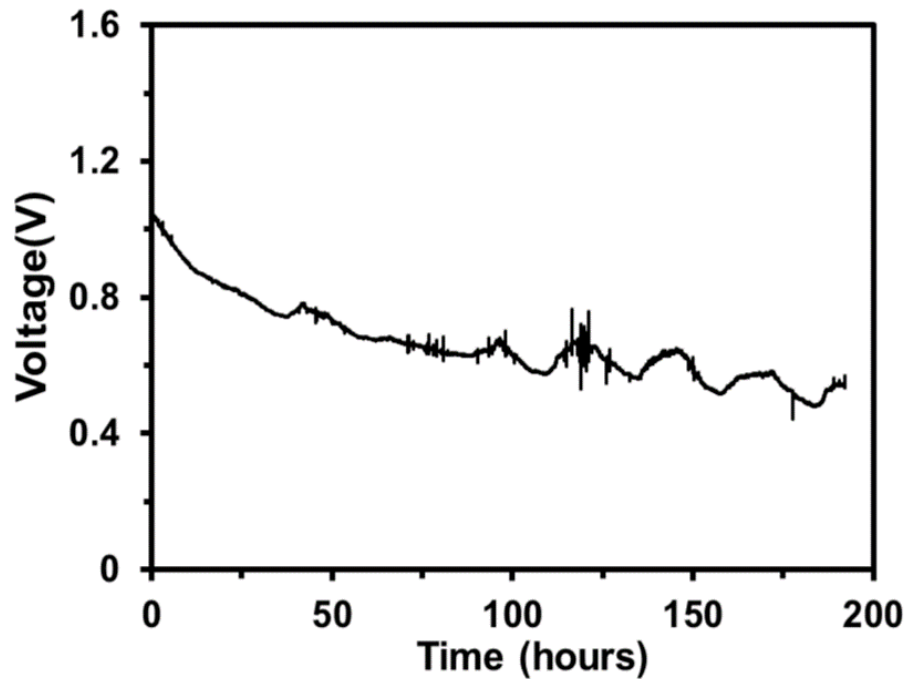
Figure 2.7. Discharge performance of Al-MOF-Air battery at current density of 100 mA/cm^2 over 200 hours under 99% humidified conditions.

The specific capacity of the AMA battery is unprecedented for any reported Al-air batteries.[84] With these characteristics, AMA batteries based on MOF crystals just few hundred microns across are able to power for hours small electronic devices such as the timers or LEDs shown in Figures 2.8.
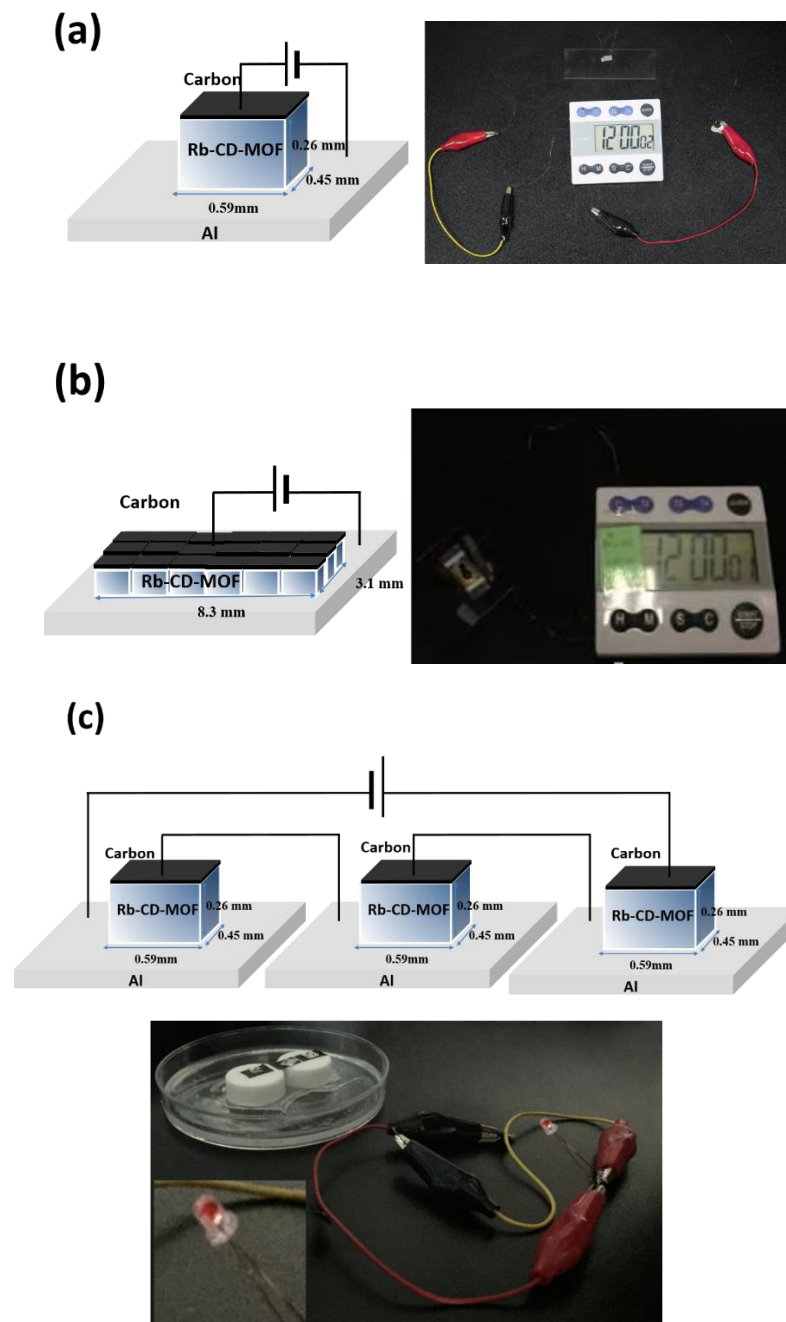
Figure 2.8. Schemes and experimental images of AMA batteries turning on various electronic devices: (a) AMA based on one MOF crystal (here, 600 μm x 450 μm x 250 μm) turns on a digital watch for ca. 30 min; (b) a dozen of similarly sized Rb-CD-MOF single crystals arranged in parallel can power the watch for about 7 hours; (c) an LED is powered for an hour with serial connection of three AMA microbatteries. The inset zooms on the LED.

To understand the mechanism underlying the operation of the AMA battery, it is important to consider the roles of the polymer/Zn NP layer, the MOF itself, and the humidity. Regarding the former, the layer of polyester on Al is known to support the transport of ions[85] (e.g., OH^- or $Al(OH)_4^-$) while minimizing the direct contact between H_2O and Al surface, so that potential-lowering hydrogen evolution reaction (HER: $2Al + 6H_2O \rightarrow 2Al(OH)_3 + 3H_2$) is repressed. This effect is illustrated in Figure 2.9 which compares RbOH-loaded MOF crystals placed on bare aluminum turning opaque, evolving hydrogen bubbles, and even cracking after ca. 30-60 min, with the same crystals placed on Al coated with the polyester/Zn NP layer, on which the crystals remain transparent with no bubbles visible.
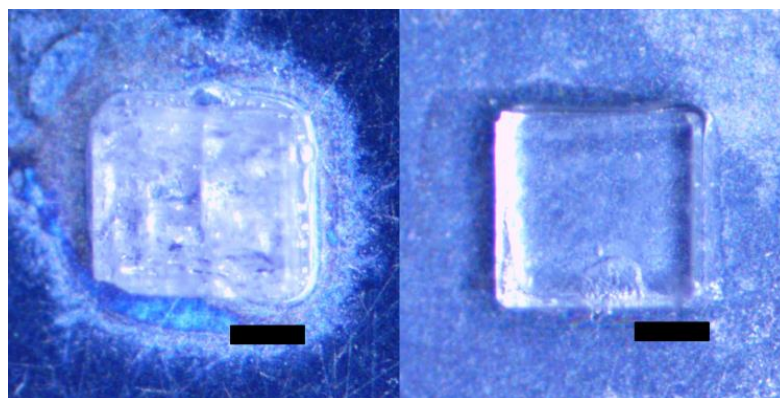
Figure 2.9. The photograph on the left shows 1M RbOH@Rb-CD-MOF single crystal placed on bare aluminum – within minutes, the crystal turns opaque and loses structural integrity. When, however, the crystal is placed on Al protected with the polyester/Zn NP layer, the crystal remains transparent. Scale bars = 100 μm.

In addition, without the polyester/Zn NP layer, the generated $Al(OH)^{4-}$ can diffuse throughout the MOF effectively making a short circuit between the Al anode and the carbon current collector. Indeed, EDS studies of the carbon electrode delaminated from the battery after discharge indicate that Al is present on this electrode when the polyster/Zn NP layer is not used; no Al signal is detected when the layer is applied. Furthermore, the Zn NPs can act as a sacrificial anode to suppress high rate of Al corrosion[86,87] ($Al(OH)_4^- \rightarrow Al(OH)_3 + OH^-$). This is confirmed by the Tafel polarization plots in Figure 2.10, from which the corrosion rate of

bare aluminum is estimated to be almost three times higher than for Al protected with polyester/Zn NP layer.
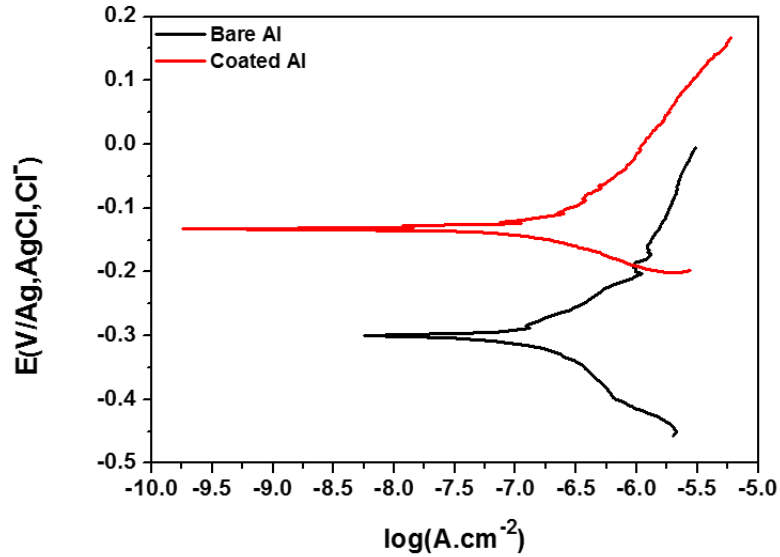
Table 1 Electochemical parameters for the Tafel plots shown in Figure 3b for the bare Al and Zn@polyester/Al (in both cases, immersed in 1M RbOH electrolyte in 3:7 v/v water/methanol mixture).

Aluminum anodes	E_{corr}(V/Ag.AgCl.Cl$^-$)	j_{corr} (A.cm^{-2})	Corrosion rate(mpy)
Bare aluminum	-0.3	0.28x 10^{-8}	0.119
Zn@ Polyester coated on aluminum	-0.13	0.85x 10^{-9}	0.037

Note: Corrosion rate can be calculated from following equation:[88]

$$\text{Corrosion rate (mpy)} = \frac{a* \ j_{corr}* \ EW}{d} \ \text{where}$$

mpy = milli-inches per year
EW = equivalent weight of the corroding species, g.
d = surface density of the corroding species, g/cm^2.
j_{corr} = corrosion current density, μA/cm^2
a = constant of corrosion rate, 0.13

Figure 2.10. Tafel-polarization curves for bare Al and for Al coated with polyester/Zn NPs layer. Measurements were performed in 1M RbOH in 3:7 v/v methanol/water mixture

Turning our attention to the role of the MOF crystal, it is not only a reservoir of ions and a medium facilitating ionic transport but, above all, acts as a bifuncional electrocatalyst supporting both oxygen reduction reaction (ORR: $O_2 + 2H_2O + 4e- \rightarrow 4OH^-$, $E^o = 0.40$ V) and the oxygen evolution reaction (OER: $4OH^- \rightarrow O_2 + 2H_2O + 4e^-$; $E^o = 0.40$ V such bifuntional ORR/OER catalysts have been of longstanding interest for the development of metal-air batteries [89],[90] We first discuss the ORR. Figures 2.11 show linear scan voltammograms (LSV).
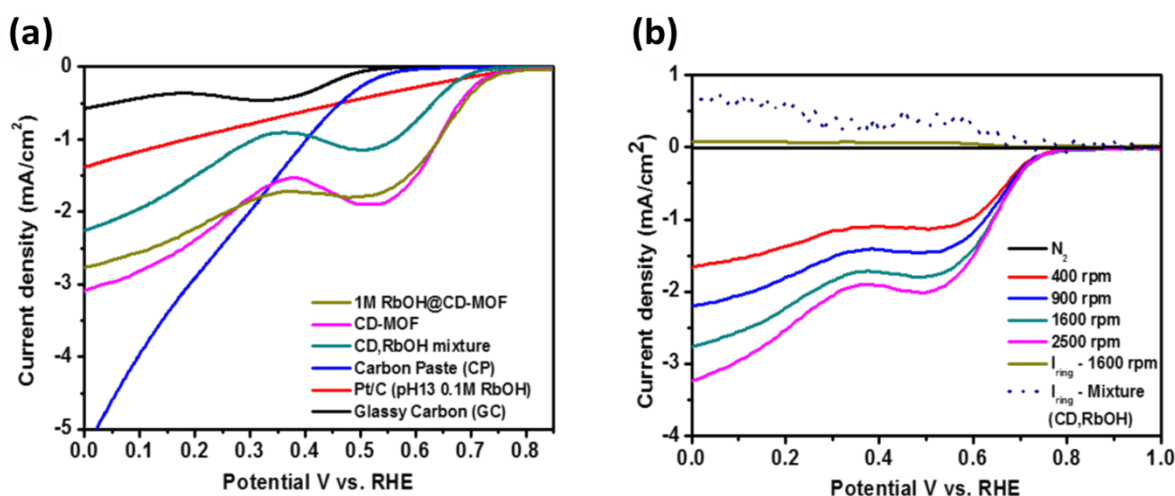
Figure 2.11. (a) Linear scan voltammograms, LSV, in the ORR region for: 1M RbOH@CD-MOF with 2 wt% carbon paste, CP, additive (khaki line); CD-MOF with 2 wt% CP (pink line); mixture of CD and RbOH powders (5mg : 5 mg) with 2 wt% CP (green line); CP only (blue line); glassy carbon (green line); and Pt/C (red line), all recored at 1600 r.p.m. with a rotating disk electrode (RDE) in O_2-saturated 0.1 M RbOH methanolic solution (Arrows indicate onset poentials). The role of the CP is to facilitate electron transport to the MOF electrocatalysts[91]; for data without the CP, see Figure S7. (b) LSV curves for 1M RbOH@CD-MOF with 2wt% CP for RDE speeds ranging from 400 to 2500 r.p.m. The ring current of ~0.05 mA/cm^2 is also plotted and compared to the much larger 0.6 mA/cm^2 ring current recorded for the mixture of the CD and RbOH powders.

characterizing the ORR performance of carbon paste (CP), glassy carbon, Pt/C powder, mixture of powdered CD and RbOH, grinded as-synthesized Rb-CD-MOFs, and grinded 1M

RbOH@Rb-CD-MOFs. As seen, powdered 1M RbOH@Rb-CD-MOFs and Rb-CD-MOFs show superior ORR performance compared to other electrodes even against Pt/C in methanolic electrolyte with positive onset potentials ~ 0.75 V vs. reversible hydrogen electrode (RHE) and a half-wave potential of 0.65 V vs. RHE. We note that the data shown was taken in 0.1 M RbOH dissolved in methanol – this choice was made to avoid dissolution of the CD-MOF crystals in pure water[78]; at the same time, experiments performed in a 10:90 v/v water/methanol mixture (see Figure 2.12) give similar results (i.e., similar onset voltages and kinetics) save higher current densities. Also of note is the fact that the CD-MOFs show superb methanol-tolerant ORR activity compared to Pt/C electrodes on which ORR is repressed due to undesirable methanol oxidation reaction, MOR, and the CO poisoning effect.[92,93]
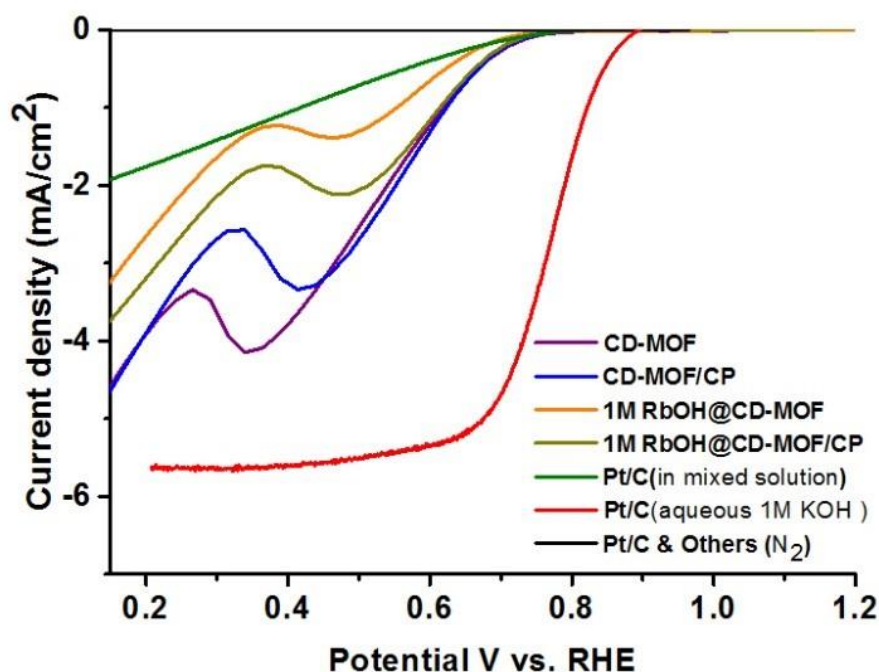
Figure 2.12. RDE polarization curves for ORR in 0.1M RbOH electrolyte in a mixture of 10% water and 90% methanol (pH = 13) with pristine Rb-CD-MOF (purple line) powder, pristine Rb-CD-MOF powder mixed with 2 wt% carbon paste (CP) as conducting addictive (blue line), 1M RbOH@Rb-CD-MOF powder (red line), 1M RbOH@Rb-CD-MOF powder mixed with 2 wt% CP (orange line), Pt/C electrode (Green line) and CP only (Magenta line). Onset potentials vs. RHE electrodes are, respectively, 0.76 V, 0.76 V, 0.67 V, 0.72 V, 0.69 V, and 0.58V. Red curve is LSV curve of Pt/C electrode in 1M KOH aqueous solution (onset potential 0.9 V). None of the electrode shows ORR performance in N_2 saturated electrolyte. The measurement of ORR behaviors was performed by RRDE at 1600 r.p.m.
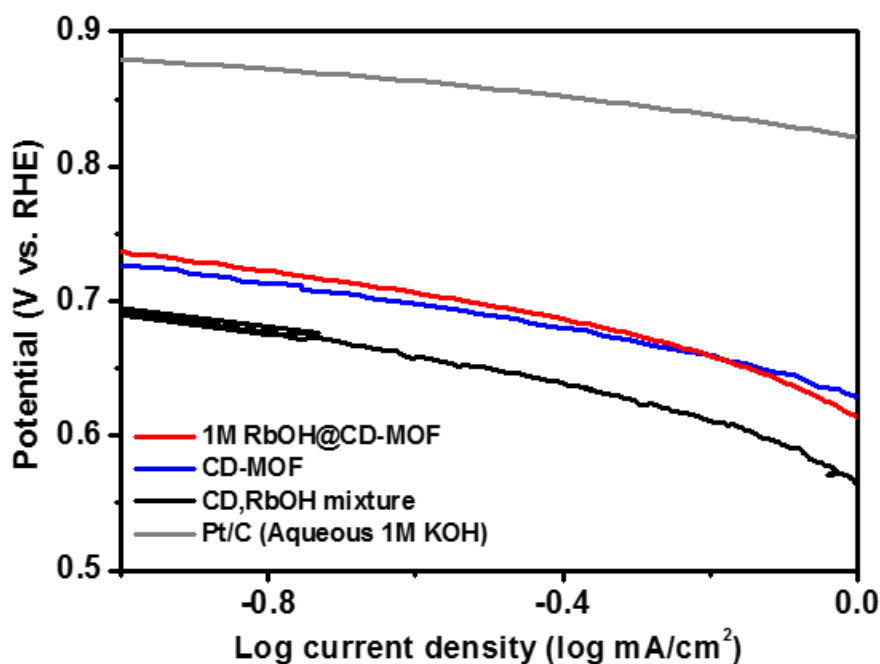
Figure 2.13. Tafel plots (log j vs potential for linear voltammetry) for select ORR data from panel (scan rate: 5 mV/s; recorded in 0.1M RbOH methnolic solution). Gray line is for Pt/C measured in 1M KOH aqueous electrolyte.

In this respect, Tafel plots in Figure 2.13 exhibit similar slopes for CD-MOFs in a methanolic electrolyte and for Pt/C electrode in an aqueous electrolyte, indicating that the former system has the ORR kinetics as good as the latter. Moreover, rotating ring-disk electrode (RRDE) measurements summarized in Figure 2.10 (b). and Figures 2.14 and figure 2.15 evidence that both native CD-MOFs and 1M RbOH@CD-MOFs exhibit high disk-current densities (~3.2 mA/cm^2) for O_2 and much lower ring-current densities (~ 100 μA/cm^2) for H_2O_2 generation; on the other hand, the mixture of CD and RbOH powders exhibits much higher ring-current densities (~ 0.6 mA/cm^2) for peroxide oxidation. These results indicate that the pathway for the generation of hydrogen peroxide ($O_2 + H_2O + 2e^- \rightarrow HO_2^- + OH^-$) is suppressed in the CD-MOFs. Indeed, estimating the number of electrons transferred per oxygen molecule, n, from the LSV curves in RRDE experiments (see SI, Section 4 for the calculations and Figure S9) gives $n \sim 3.75$ for both CD-MOFs and 1M RbOH@CD-MOFs (with carbon, but only $n = 2.25$; for CD-RbOH mixed powders – in other words, the MOFs are performing close to the ideal ORR, four-electron-transfer limit.
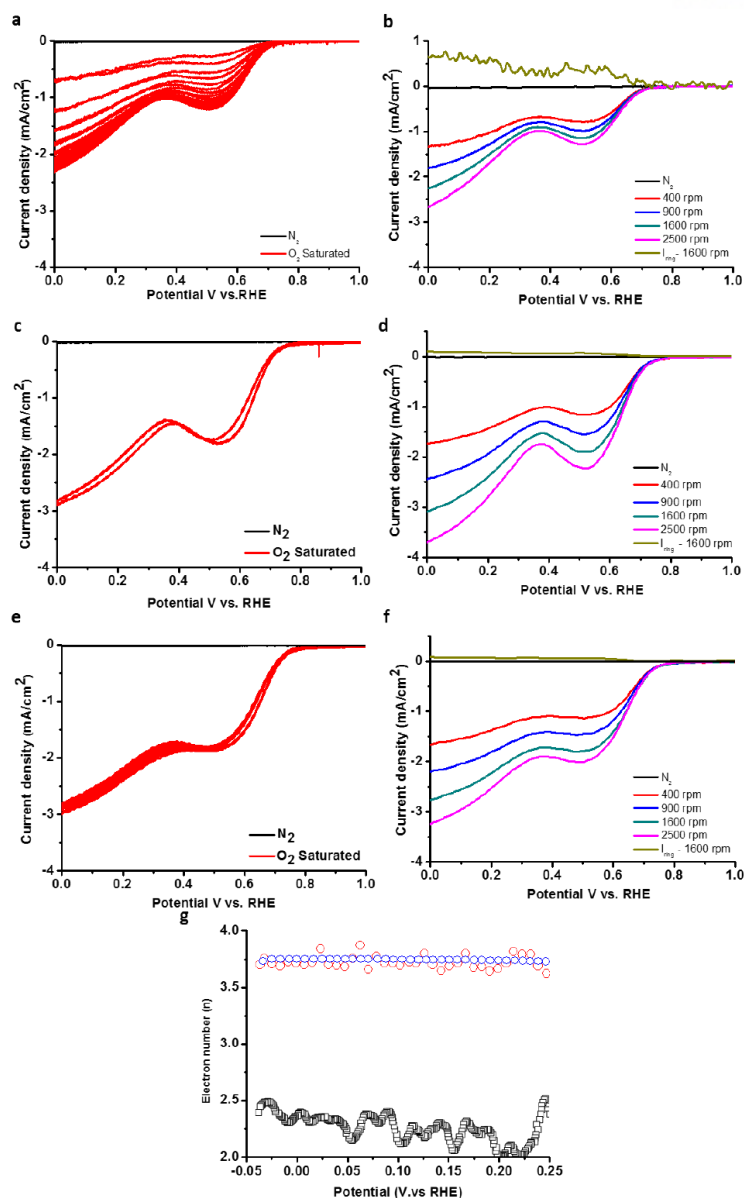
Figure 2.14. The ORR characteristics with a 2 wt% conductive CP additive for **(a,b)** a CD and RbOH mixture powder (1mmol γ-cyclodextrin (1.03 g) and 4 mmol rubidium hydroxide hydrate (0.41 g)); **(c,d)** pristine Rb-CD-MOF powder; and **(e,f)** 1M RbOH@CD-MOF powder mixed with 2 wt% of carbon paste as a conducting additive in 0.1M RbOH methanolic solution. The plots are for rotational speeds of the RRDE ranging from 400 rpm to 2500 r.p.m. Characteristics under oxygen and nitrogen are also included. The plots **(b,d,f)** evidence that I_r currents for Rb-CD-MOF and 1M RbOH@Rb-CD-MOF are much lower (approximately 100 $\mu A/cm^2$ at 0 V vs. RHE) than for the mixture of CD and RbOH (0.6 mA/cm^2). Furthermore, plots in **(c,e)** indicate that the Rb-CD-MOF and 1M RbOH@Rb-CD-MOF retain stable ORR behavior . On the other hand, the mixture of CD and RbOH does not give stable ORR cycles in CV (plot in **a**). **(g)** Dependence of the electron transfer number, n, on the potential for 1M RbOH@ Rb-CD MOF, Rb-CD MOF, and mixture of CD and RbOH. 1M RbOH@Rb-CD-MOFs shows the most efficient ORR process, with the highest number of electrons transferred, $n = 3.75$ (cf. $n = 3.72$ for pristine Rb-CD-MOF and $n = 2.4$ for the mixture of CD and RbOH).
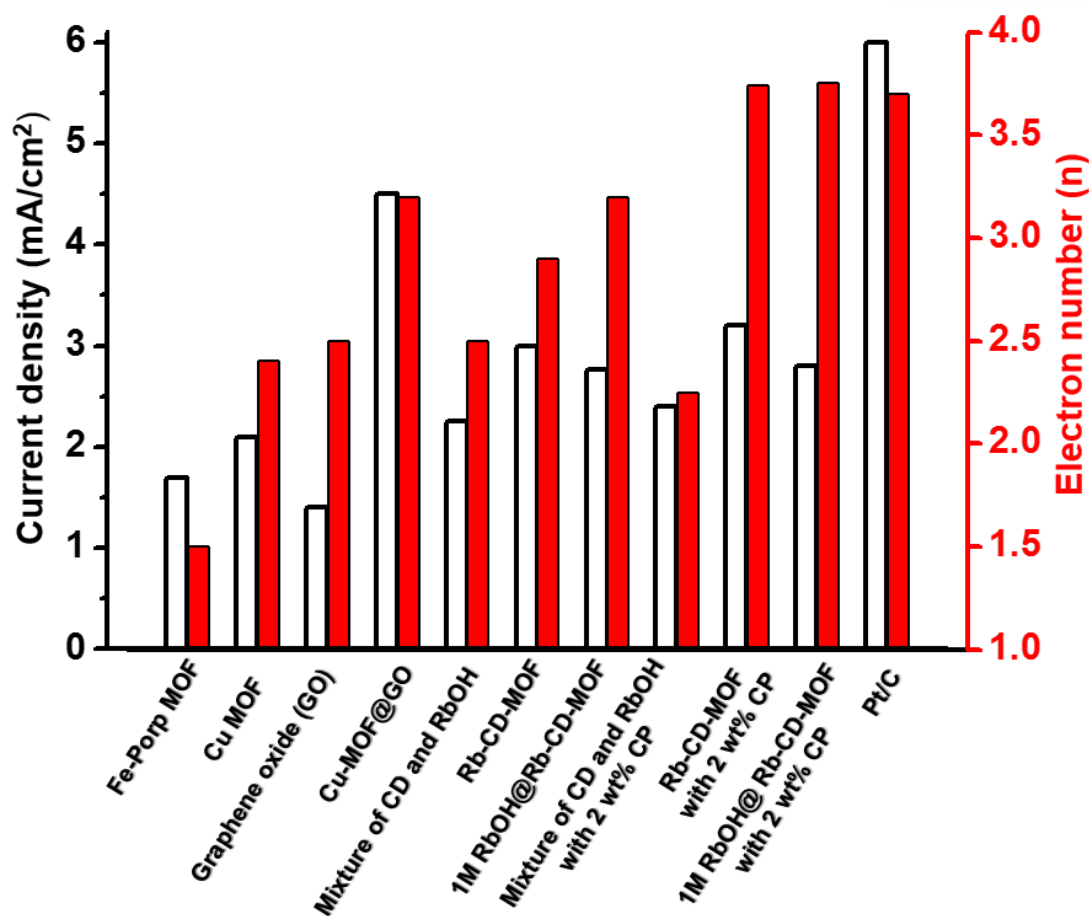
Figure 2.15. The histogram gives the values of the number of electrons transferred, *n* (red bars) and electrochemical activity (given as the fully diffusion-limited current density, j_L, at 0 V vs. RHE; empty bars) for ORR performance of reported MOFs[94,95], mixtures of CD and RbOH, and Rb-CD-MOFs with and without the RbOH electrolyte. Note: The comparison for the ORR electrocatalytic performance is for pristine MOFs not carbonized MOFs (e.g., ref 9; ORR catalyst based on Fe-P MOF composite, ref 10; ORR catalyst based on Cu MOF, GO, and Cu MOF@GO).

Finally, the K-L plots in Figure 2.16 show linear relationship between the inverse kinetic current, j_k^{-1}, and the inverse square root of the electrode's angular velocity, $\omega^{-1/2}$, which is typical for first-order reaction kinetics with respect to the diffusion of O_2 into the electrocatalysts.[96] Lower slopes of such dependencies indicate faster kinetics. participating in the ORR – reassuringly, the slope of 1M RbOH@CD-MOF is lower (9.13) than the slopes for either pristine Rb-CD_MOF (11.20) or mixture of CD and RbOH powders (12.22).
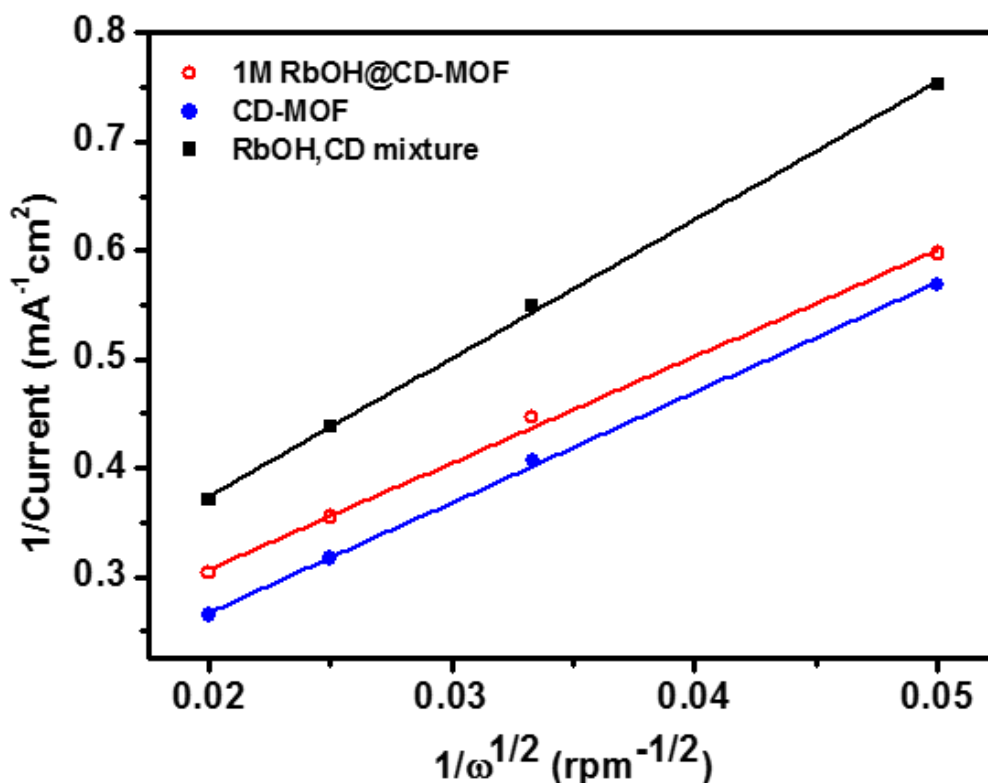
Figure 2.16. Corresponding K-L plots j^{-1} vs. $\omega^{-1/2}$, where j denotes current density and ω angular velocity of the RDE.

Overall, the efficient, almost four-electron ORR performance of CD-MOFs can be reasonably ascribed two interrelated effects: (1) the presence of open Rb^+ coordination sites[97] binding O_2 and H_2O and, as suggested in previous works[98], capable of making rubidium superoxide ($[Rb^+\text{-}O_2^-]$), which can be an intermediate in oxygen reduction; and (2) hydrophilic nature of channels within Rb-CD-MOF monocrystals facilitating adsorption of O_2 and H_2O "fuels" for ORR, and enabling their long-range transport (i.e., without clogging or through grain boundaries, as in the much less efficient CD-MOF powders.[99] Together with the corrosion of Al, the ORR reaction completes the net electrochemical reaction of the AMA battery as follows: $4Al + O_2 + 6H_2O + 4OH^- \rightarrow 4Al(OH)_3$ $\quad E_0 = 2.75$ V (eq.1) (Fig. 1f).

In addition to these two processes, MOF crystals also support the oxygen evolution reaction (OER: $4OH^- \rightarrow O_2 + 2H_2O + 4e^-$), as evidenced by the rapid increase of anodic current in the LSV curve extended into the OER region (above ~ 1.40 V vs. RHE, **Figure 2.16-a**).The

slopes of the Tafel plots in **Figure 2.16-b** indicate that the catalytic activity and kinetics of 1M RbOH@CD-MOF are better than for as-synthesized CD-MOF or CD-RbOH powder mixture, better compared to many other reported electrodes electrodes (Fe-MOF, Cu-MOF, graphene oxide,GO, and chemical mixture of Cu-MOF and GO, see Figure S9), and comparable with the characteristics of the Pt/C loaded electrode. While the role of OER is not as clear as that of ORR, the discharge experiments described below suggest that it might be important for the regeneration of the water and oxygen "fuels".
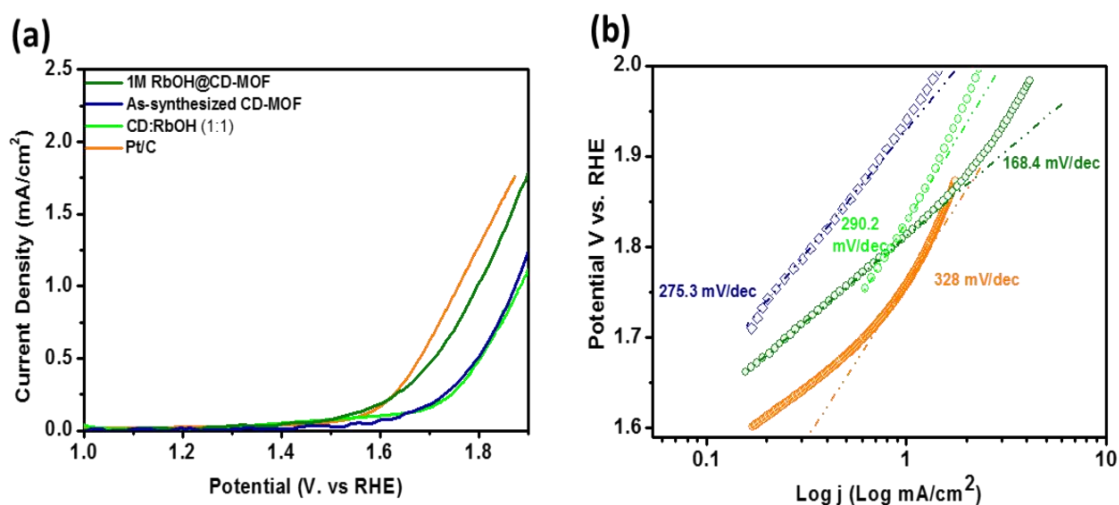
Figure 2.16 (a) LSV curves for the OER performance, all recorded in N_2-saturated 0.1M RbOH electrolyte. (b) Corresponding Tafel plots of the OER.

In this context, Figure 2.17 illustrates the performance of the AMA battery under 10^{-3} mTorr vacuum, with no inflow of water and oxygen. Interestingly, the battery still operates though the potential drops more rapidly (from ~ 1.4 V to ~ 0.4 V at 100 mA/cm^2 discharge current) than under humidified conditions (compare with Figure 2.6).
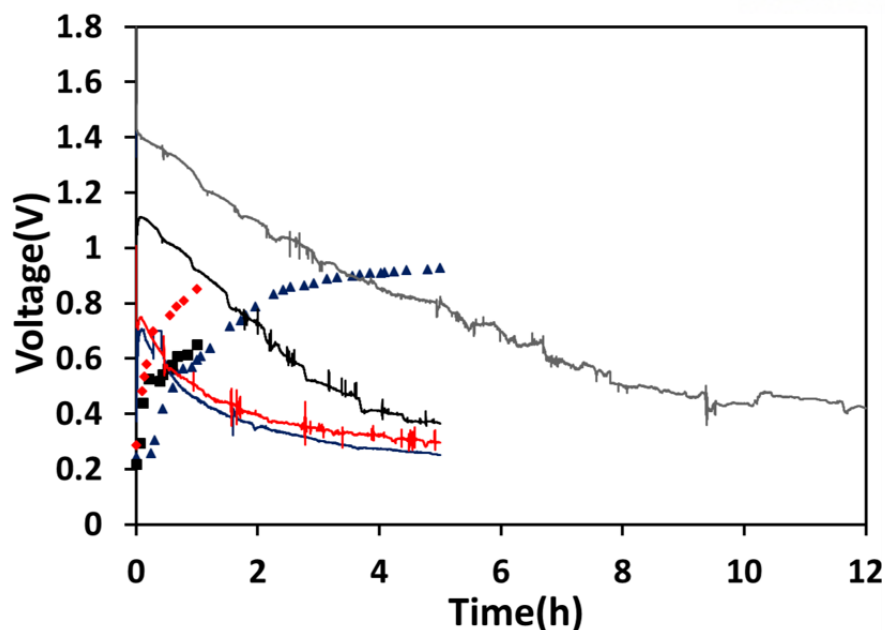
Figure 2.17 Discharge curves of the AMA battery under vacuum (10^{-3} mTorr). Gray, black, red and blue are, respectively, the first, second, third, and fourth discharge curves with 100 mA/cm^2 discharge current. Black, red, and blue dots are, respectively, first (1 hr), second (1hr) and third (5hrs) charging curves.

It is reasonable to assume that the ORR assists in this operation by utilizing adsorbed water and oxygen in the single crystal MOF and regenerating oxygen inside from the hydroxide anions present inside of the crystal. Moreover, the potential can be recovered again when the battery is exposed to water vapor (note: typically, the vapor is obtained by bubbling air through a 3:7 v/v mixture of water and methanol; while methanol does not play the role as fuel, there is no methanol oxidation peak which can be observed from ~ 1.4 V to ~ 1.6 V vs RHE in Fig 3g[100], such a mixture is not causing crystal's dissolution, as can happen over time in pure water). Interestingly, the battery cannot be recharged electrically as high reduction potential required for reducing Al(OH)$_3$ to Al this observation suggests that the ORR and OER might occur at separate locations within the MOF, as previously suggested for a construction model of bifunctional oxygen electrodes[101] and illustrated in Figure 2.18.
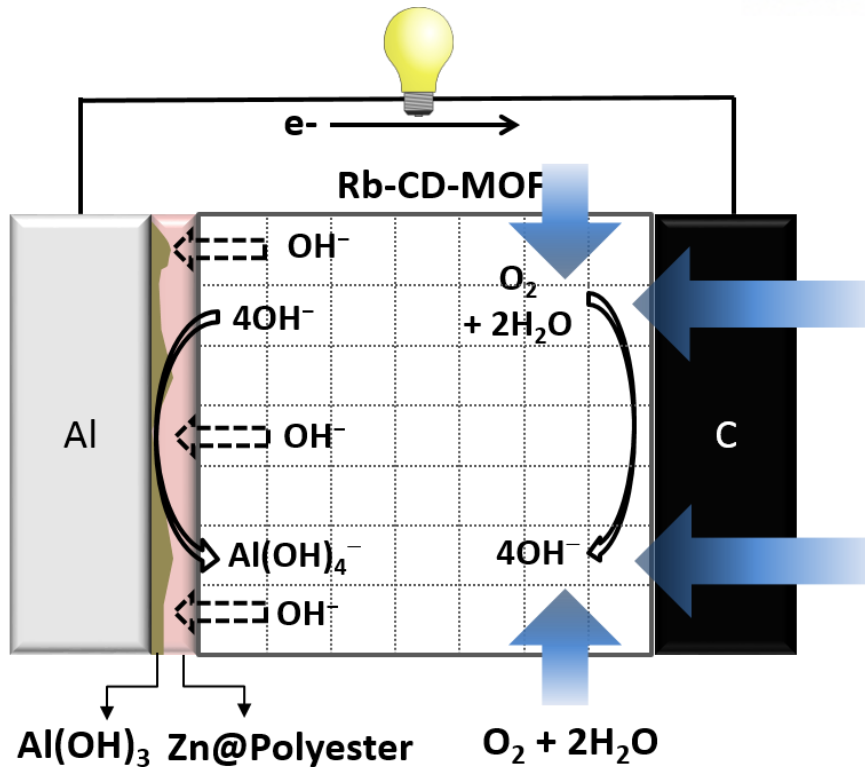
Figure 2.18. Scheme of the AMA battery and the key chemical processes underlying its operation.

Specifically, the ORR should take place predominantly at the interface between the MOF crystal and the carbon electrode and the OER, close to the Al electrode with discharge current creating internal electrical potential therein. The OH⁻ generated by the ORR can help dissolve the $Al(OH)_3$ passivation layer formed on the Al surface by the anodic oxidation (Fig 2.19),
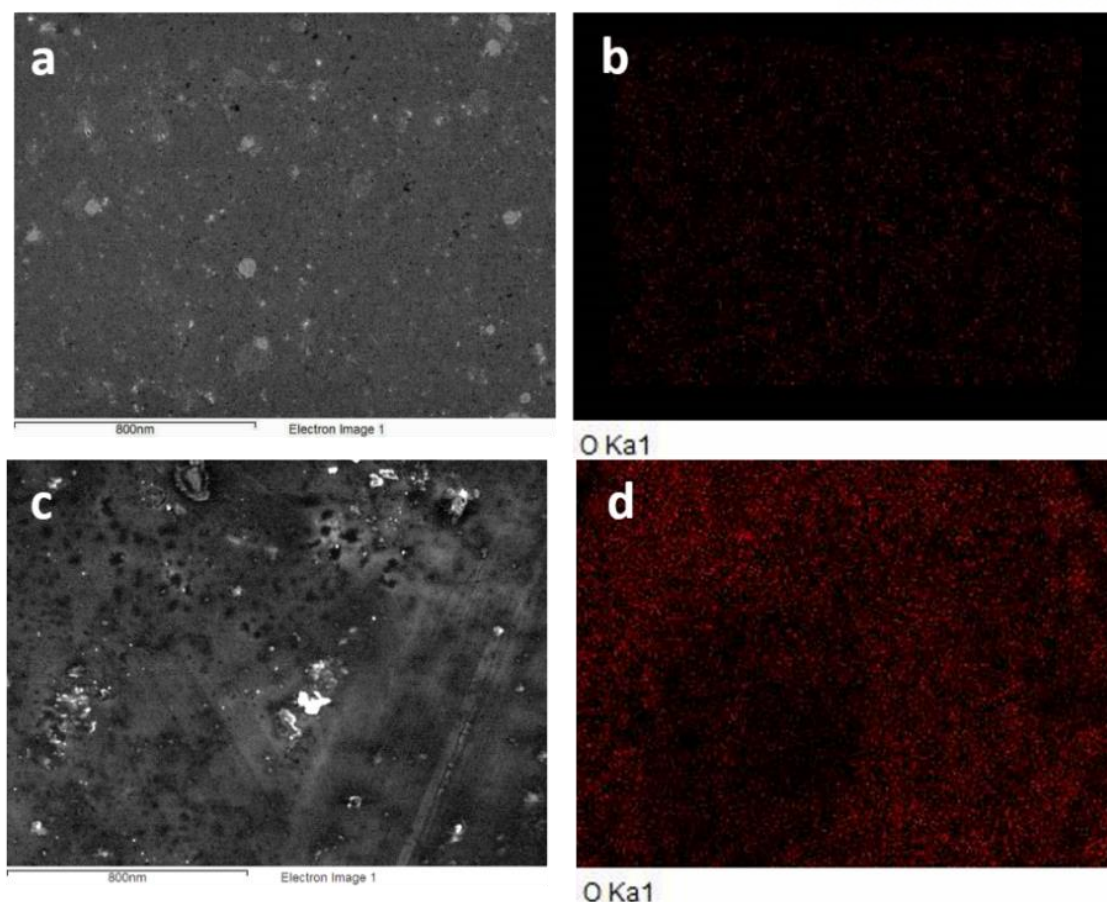
Figure 2.19. SEM images of Al surfaces and EDS spectra mapping for oxygen contents on the Al surfaces (**a,b**) before discharge and (**c,d**) after discharge of the AMA battery. Appearance of a porous surface and increase of oxygen content after battery discharge indicate that Al surface is oxidized forming $Al(OH)_3$ during the discharge process.

Interestingly, the fluctuations in the discharge curves in Figures 2.6 and 2.17 point to a cyclic nature of $Al(OH)_3$ formation and its subsequent dissolution by OH^- ions – as, indeed, described earlier works[102] Additional evidence for the dissolved Al comes from the elemental mapping indicating Al being present in the Rb-CD-MOF single crystal (Figure 2.20).
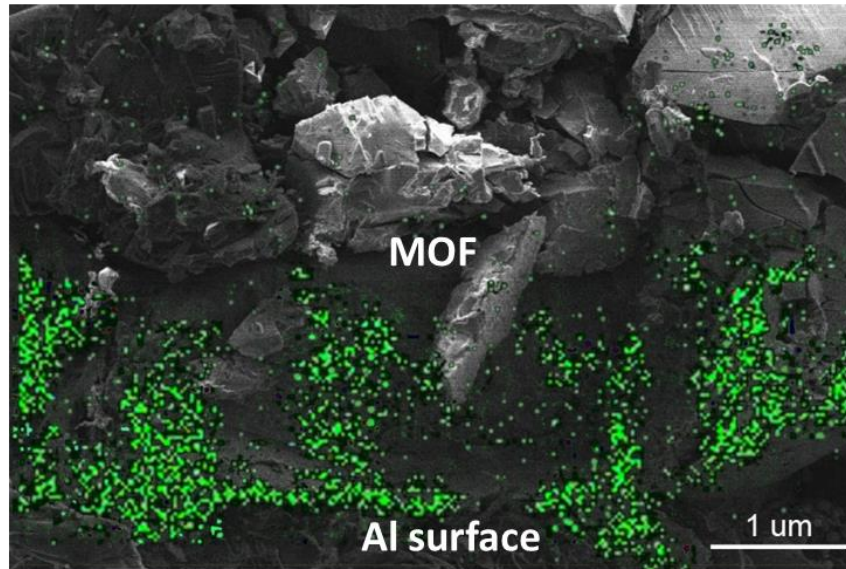
Figure 2.20. SEM image within cross-section view of artificially sheared Rb-CD-MOF single crystal adjacent to Al anode and EDS mapping for Al (green dots). Inset scale bar denotes 1 μm

Additional experiment *1*. Further characterization of the Zn@polyester layer and its role as corrosion-inhibitor/separator.
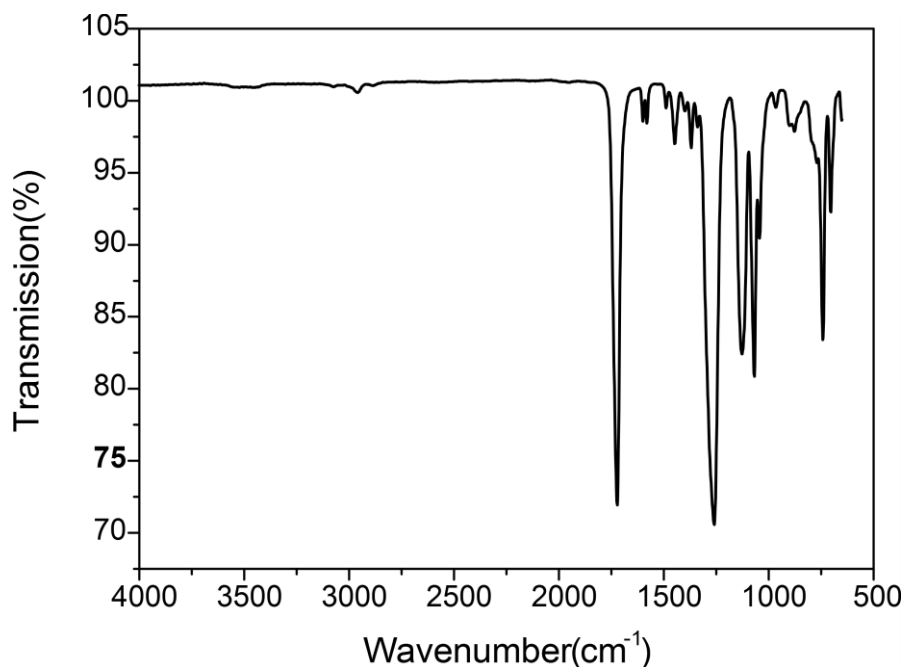
Figure 2.21. FTIR spectroscopy of the polyester layer with embedded Zn nanoparticles (Zn@polyester) and coated on Al surface (cf. Section S1). The strong 1722 cm^{-1} C=O stretch is due to ester groups and the weak O-H stretch around 3500 cm^{-1} due to OH's, indicating linear-type polyester.[103,104]
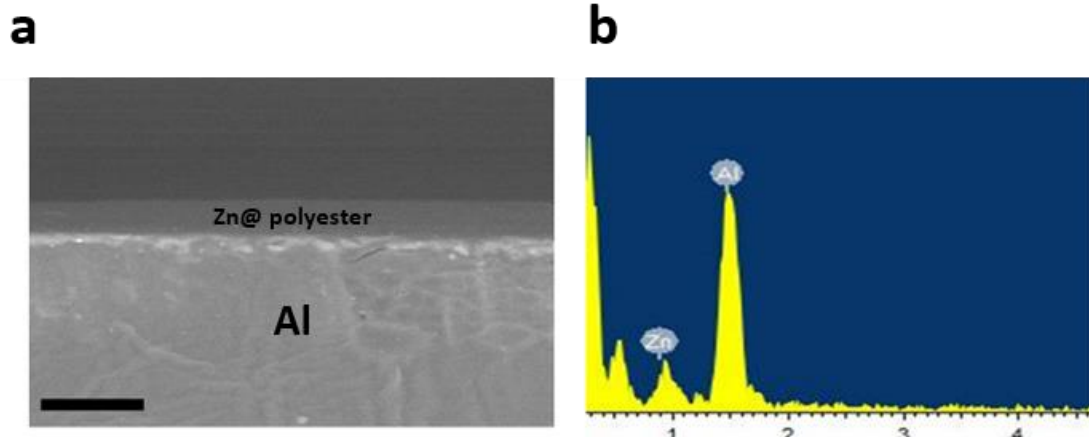
Figure 2.22 (a) Cross-sectional SEM image and **(b)** energy dispersive spectrum (EDS) of the Zn@polyester layer coated on Al.
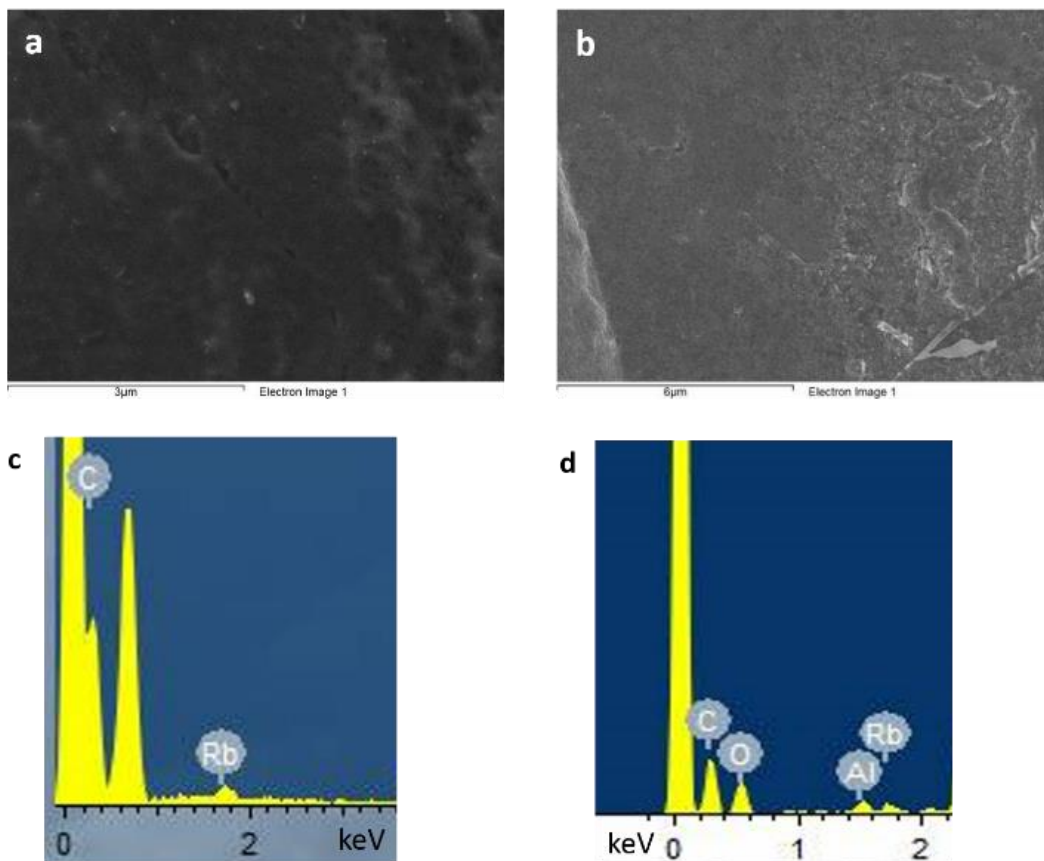
Fig. 2.23. SEM image of the "top" carbon electrode delaminated from **(a)** AMA battery with Zn@polyester layer coated on the Al anode and **(b)** AMA battery with just bare Al anode, not coated with Zn@polyester. The corresponding EDS spectra in **(c,d)** indicate that no Al is present on the carbon electrode only if the Zn@polyester separator is used.

Additional experiment *2*. Additional considerations for the oxygen reduction reaction (ORR) and the oxygen evolution reaction (OER).

Electrode preparation

Catalyst inks were prepared by dispersing grinded MOF single crystals (10 mg) in 450 µL of methanol, and adding 50 µL of 5 wt. % nafion solution (Sigma-Aldrich 274704). In order to increase diffusion-limited current density (j_L) of the catalysts, 2 wt% carbon paste was added as a conducting agent. 5 µL of the catalyst ink thus prepared was dropped onto the ring-disk electrode, and then dried at ambient conditions.

Electrochemical characterization

Cyclic and linear sweep voltammograms (CVs and LSVs) were obtained on disk and ring electrodes simultaneously by a potentiostat (PARSTAT MC, Princeton Applied Research). Ring-disk electrodes (RRDE) of glassy carbon disk and platinum ring was used as the working electrode (disk area = 0.125 cm^2) while a platinum wire and a Ag/AgCl electrode were used as the counter and reference electrodes, respectively. The RRDEs were rotated at various controlled speeds (1600 r.p.m. unless otherwise indicated) by a RRDE controller (ALS RRDE-3A). An aqueous solution of 0.1M RbOH as the electrolyte is isostructural system with MOF battery. Encapsulated RbOH can be anchored at the ligand of cyclodextrin walls in MOFs by coordination between Rb+ and the hydroxyl groups. ORR and OER polarization curves were obtained on the disk electrode from a cathodic sweep from +0.1 V to -0.7 V (vs. Ag/AgCl) at 10 mV s^{-1} after twenty cycles of CVs (Figure 3c,3g, S6, S7a-c, and S8). The electrolyte was saturated by oxygen for ORR and was purged with nitrogen to measure background currents. +0.4 V was applied to the ring electrode to estimate the amount of peroxide generated from the disk electrode. The values of potential were converted from "vs. Ag/AgCl" to "vs. the reversible hydrogen electrode (RHE)" by: $E_{RHE} = E_{Ag/AgCl} + 0.059pH + E_{0(Ag/AgCl)}$ (0.1976 V at 298 K).

Number of electrons transferred (n)

There are two kinds of ORR behaviors (4e$^-$ and 2e$^-$ ORR processes). The disk current (I_d or I_{disk}) can result from both 4e and 2e ORR. Hydrogen peroxide (HO$_2^-$) can be produced from the 2e ORR process, which is detected on the ring electrode (as I_r or I_{ring}) by re-oxidizing the hydrogen peroxide. Therefore, both *n* (number of electrons transferred) and the amounts of peroxide production (HO$_2^-$ %) are easily determined by comparing the values of I_d and I_r via the following equations:

$$n = 4 \frac{I_d}{(I_d + \frac{I_r}{N})}$$

$$HO_2^- (\%) = 200 \frac{\frac{I_r}{N}}{I_d + \frac{I_r}{N}}$$

where N is the collection efficiency measuring the fraction of hydrogen peroxide produced on the disk electrode to be detected on the ring electrode.

The value of N for the RRDE we used was measured by using 10 mM aqueous electrolyte of potassium ferricyanide ($K_3[Fe(CN)_6]$) in 0.1M KOH in a three-electrode configuration (RRDE as the working electrode, Pt wire as the counter electrode, and Ag/AgCl as the reference). The disk potential was swept from 0.6 V to -0.5 V at various rotating speeds while the ring potential was fixed at 0.6V. The value of $N = 0.412$ was estimated from the ratio of the limiting ring current to the limiting disk current (note: this value was close to the theoretically calculated value of 0.424 based on the dimensions and geometry of our RRDE).

The calculated values of n are summarized in Figure S9. The value of n approaching 4 means less generation of hydrogen peroxide and preference for a one-step process to generate OH^- (i.e., akin to Pt).

Koutecky-Levich (K-L) equation

The kinetic parameters of ORR can be analyzed on the basis of the K-L equations. The linearity in diffusion-limiting current (j_L) vs. square root of rotation rate ($\omega^{-1/2}$) (Fig. 3f and Fig. S7d) signifies a simple and reversible half-reaction without complications due to sluggish kinetics or coupled chemical reactions.

$$\frac{1}{j} = \frac{1}{j_K} + \frac{1}{j_L} = \frac{1}{j_K} + \frac{1}{B\omega^{1/2}}$$
$$B = 0.2nF(D_{O_2})^{\frac{2}{3}} \; \gamma^{-1/6}C_O$$
$$j_K = nFkC_O$$

where j = the measured current density, j_K = the kinetic limiting current density, j_L = the diffusion-limiting current density, ω = the angular velocity of the rotating disk, n = the overall number of electrons transferred in ORR, F = the Faraday constant, C_O = the bulk concentration of O_2, D_0 = diffusion coefficient of O_2, γ = the kinematic viscosity of the electrolyte, and k = the electron transfers rate constant.

Tafel equation

From the Tafel plot and equation (Fig. 3e and f), the slope (b) and other important kinetic parameters can be determined. Lower slopes correspond the faster kinetics.[105]

$$\eta = a + b\log(i)$$

$a = RT\ln i_0/(\alpha \, n_{RDS}F)$; $b = -2.3RT/(\alpha \, n_{RDS}F)$; η = overpotential; i = current; i_0 = exchange current; n_{RDS} = number of electrons transferred in RDS; α = transfer coefficient, F = faradaic constant (96485 C/mol) R = ideal gas constant (8.314 J/mol K); T= absolute temperature (K).
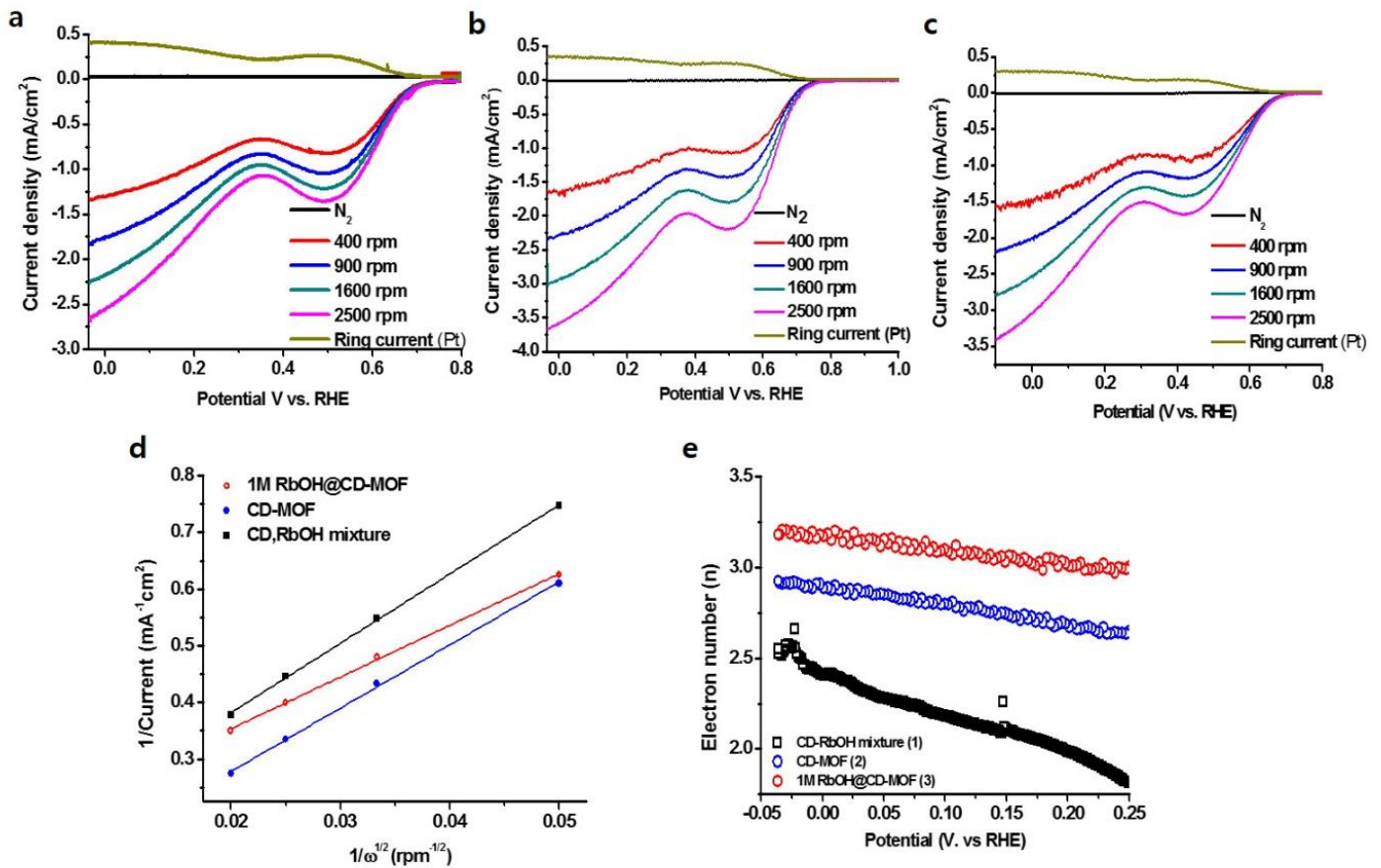
Figure 2.24. The ORR performance (without conducting CP additive) of **(a)** mixture of CD and RbOH (1mmol γ-cyclodextrin (1.03 g, >98 %, TCI) and 4 mmol RbOH rubidium hydroxide hydrate (0.41 g, 85%, Sigma Aldrich)); **(b)** Rb-CD-MOF, and **(c)** 1M RbOH@CD-MOF in 0.1M RbOH methanolic solution all at rotational speeds of the RRDE ranging from 400 r.p.m. to 2500 r.p.m. Note that the mixture of CD and RbOH exhibits higher ring current (I_r, 0.4 mA/cm^2) than either pristine Rb-CD-MOFs (I_r = 0.28 mA/cm^2) or 1M RbOH@Rb-CD-MOFs (I_r = 0.25 mA/cm^2). **(d)** The Koutecky-Levich, K-L, plots (jk^{-1} vs $\omega^{-1/2}$) at various electrode potentials exhibits good linearity[5]. **(e)** 1M RbOH@Rb-CD-MOFs shows the most efficient ORR process with the highest number of electrons transferred among the catalysts without carbon addictive, n = 3.23 (vs. n = 2.9 for pristine Rb-CD-MOF and n = 2.5 for the mixture of CD and RbOH).

Section 5. Additional data on the performance of Al-MOF-air batteries.
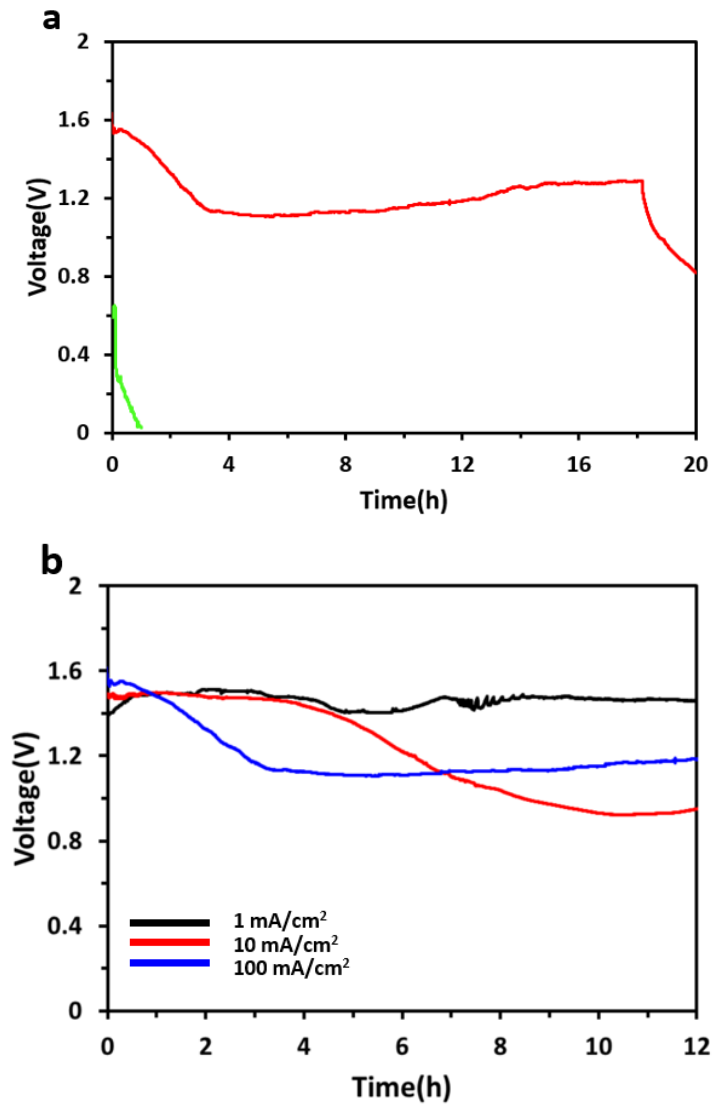
Figure 2.25. (a) Discharge characteristics of (red line) the AMA battery under 99% humidified conditions with 100 mA/cm^2 discharge current and (green line) Al-air battery fabricated with glass filter paper instead of a MOF single crystal and with 10 mA/cm^2 discharge current. **(b)** Discharge performance of the Al-MOF-Air battery at current densities of 1 mA/cm^2, 1 mA/cm^2, and 100 mA/cm^2.

2.3 Conclusion

we have described a new type of an aluminum-MOF-air battery whose key element is a single crystal MOF crystal supporting both ORR and OER processes powered by oxygen and water fuels. The combination of MOF's porosity, its bifunctional catalytic properties, and suppression of anode oxidation result in the battery's very high discharge capacity, $> 15,000$ mAh/cm^2. From a practical point of view, the AMA battery is interesting because it enables an efficient use of the abundant Al metal and platinum-group free air cathode (platinum-group metals have widely used as catalysts for ORR and OER in air-cathode of metal-air batteries). Currently, the sub-millimeter crystals we use point at microbattery applications. However, our recent effort in large area (up to six-inch wafers), freestanding MOF films[106] as well as the growth of large (up to cm) single crystals of CD MOFs[107] suggest possible scale-up of the concepts we described here.

2.4 Experimental section

Synthesis of Rb-CD-MOF single crystals

In a scintillation vial, 1 mmol γ-Cyclodextrin (1.03g, >98 %, TCI) and 8 mmol Rubidium hydroxide hydrate (0.82 g, 85%, Sigma Aldrich) were dissolved in 20 mL of deionized (DI) water by sonication for 10 minutes. The clear solution was divided evenly into 5 prewashed vials (4 mL per vial). Methanol (ca. 50 mL) was allowed to vapor diffuse into the vials slowly over a period of 4 days. From submillimeter- to millimeter-sized (up to ca. 2*2*1 mm), colorless cubic Rb-CD-MOF single crystals were produced in the vial (Fig. 1c).[108][109]

Preparation of Al anodic electrode

To prepare flat and clean aluminum anode, aluminum surface (99.99%, 0.25 mm thickness, Sigma Aldrich) was grinded with sandpapers which grit size of P1200 and P4000 sequentially, then polished with discs of micro abrasive wetted with diamond suspension (diameter of diamond particles is ca. 3 ~ 9 μm, PRESI) and lubricant (PRESI). The diamond suspension and lubricant stained Al electrode was washed with DI water and acetone. The grinding and polishing process were performed by polishing machine (Mecatech 234, PRESI).

In order to deposit layer of zinc nanoparticles (NPs) embedded polyester (Zn NPs@polyester) as a corrosion inhibitor and separator on the polished Al electrode, following preparation steps were required: 6 wt% mounting wax in 10 mL acetone and zinc nanopowder (20mg, <50nm particle size, ≥99%, Sigma Aldrich) was added in the solution. 2) To disperse the zinc NPs in acetone, the mixed solution was stirred for 24h and then, aggregated particles were filtrated by syringe filter (PTFE, average pore size: 0.45 μm, Fluoropore™). 3) The polished aluminum foil was put into the solution for 1h and washed by isopropanol and DI water alternately, then dried by blowing nitrogen gas. In this step the Zn NPs@polyester film was deposited on the polished Al. 4) The Zn NPs@polyester coated Al was immersed into 0.1M potassium hydroxide (0.048g, ≥85%, Sigma Aldrich) aqueous solution for 30s. The thickness of Zn NPs@polyester layer on Al is around 10 μm in thickness which was confirmed by a Scanning Electron Microscope (S-4800, Hitach High-Technologies).

Fabrication of Al-MOF-air battery

A single crystal of Rb-CD-MOF was sandwich packed with Zn@polyester coated Al electrode and conductive carbon paste (TED PELLA) (Figure S5). Mostly selected MOF single crystals' size were ca. 300 μm: 300 μm: 50 μm = width: length: thickness for the Al-MOF-air battery fabrication. For stable positioning of the MOF single crystal on the Al electrode, the MOF crystal was fixed by plastering epoxy (Araldite) only two side walls of the single crystal (Other faces of the cubic single crystal were utilized as channels for water and oxygen adsorption). Each end of the electrodes (Al and carbon) were connected with copper wire (0.001 in diameter, Alfa Aesar). In order to dry the carbon paste and harden the epoxy, the Al-MOF-air cell was heat at 65℃ for 1 hour. Before performing electrochemical measurements, the baked Al-MOF-air cell was filled out vapor from mixed solvent with 70 % methanol and 30 % DI water for an hour with dry air.

Electrochemical measurements

Electrochemical measurements were performed at room temperature using potentiostat (PARSTATMC, Princeton Applied Research) instrument with VersaStudio ™ analyst software.

Performances of Al-MOF air battery were tDested in Schleck flask connected with vaporizing system or vacuum. Fig. S1.

Tafel plots of bare aluminum and Zn NPs@polyester coated aluminum were obtained from Al electrodes as a working electrode, Ag/AgCl as a reference electrode, and platinum wire as a counter electrode. The surfaces were exposed to 0.6 wt% NaCl in aqueous solution (pH 5.6). Scan rate is 5 mVs^{-1}.[110]
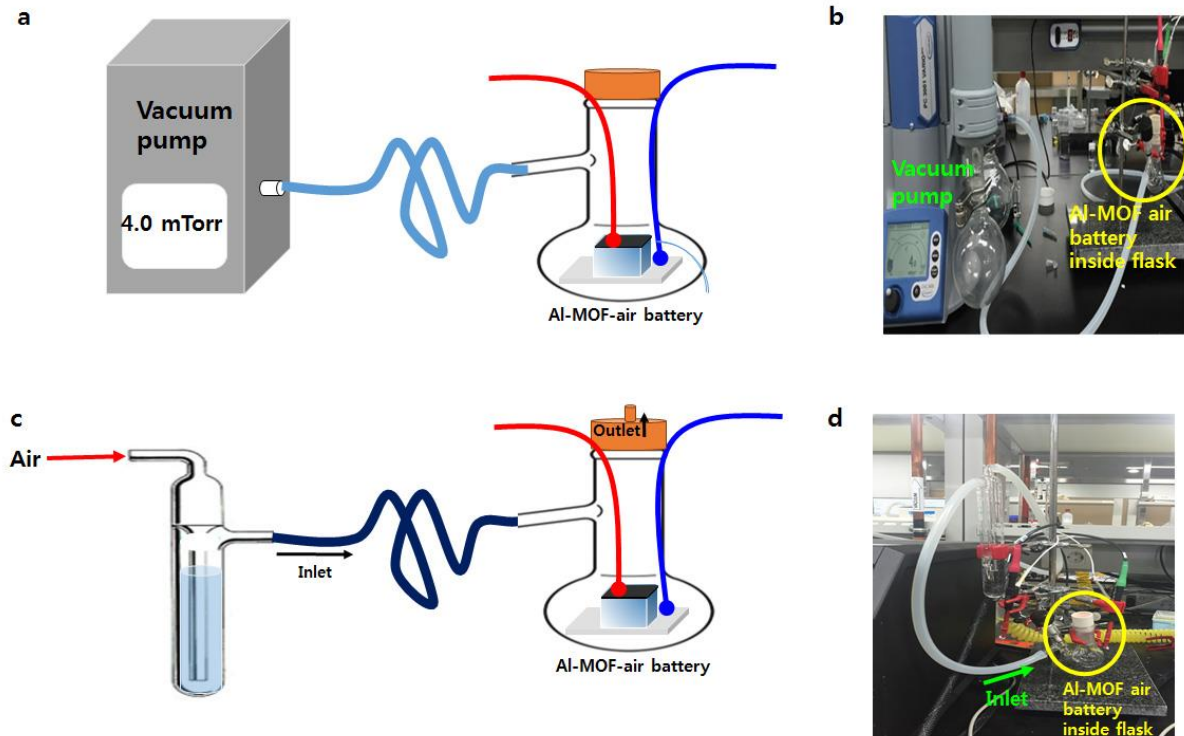
Figure 2.26 Schematic views and photographs of set up for Al-MOF- air battery. (A and B) For measurement of Al-MOF-air battery perfomance under 4 mTorr vacuum condition and (C and D) under 99% humidified condition with injection of vapor from methanol and water mixture (methanol:water = 70:30).

References

[1]. M. Mokhtar *et al.,* Recent developments in materials for aluminum-air batteries: a review. *J. Ind. Eng. Chem.* **32**, 1-20 (2015).

[2]. Q. Li, N. J. Bjerrum, Aluminum as anode for energy storage and conversion: a review. *J. Power Sources* **110**, 1-10 (2002).

[3]. M. A. Rahman, X. Wang, C. Wen, High energy density metal-air batteries: A review. *J. Electro. Soc.* **160**, A1759-1771 (2013).

[4]. M. C. Lin *et al.* An ultrafast rechargeable aluminum-ion battery. *Nature* **520**, 324-328 (2015).

[5]. F. Presuel-Moreno, M. A. Jakab, N. Tailleart, M. Goldman, J. R. Scully, Corrosion-resistant metallic coatings. *Mater. Today* **11**, 14-23 (2008)

[6]. P. Karlsson, A. E. C. Palmqvist, K. Holmberg, Surface modification for aluminum pigment inhibition

[7]. D. Wong, F. H. Cocks, The use of zinc to control aluminum corrosion in aqueous glycol solutions. Corrosion. **36**, 587-591 (1980)

[8]. S. Han *et al.* Chromatography in a single metal-organic framework (MOF) crystal. *J. Am. Chem. Soc.* **132**, 16358-16361 (2010)

[9]. S. Bai, X. Liu, K. Zhu, S. Wu, H. Zhou, Metal-organic framework-based separator for lithium-sulfur batteries. *Nat. Energy* **1**, 16094 (2016)

[10]. J. Zhang, Z. Zhao, Z. Xia, L. Dai, A metal-free bifunctional electrocatalyst for oxygen reduction and oxygen evolution reactions. *Nat. Nanotech.* **10**, 444-452 (2015)

[11]. B. Y. Xia et al. A metal-organic framework-derived bifunctional oxygen electrocatalyst. *Nat. Energy* **1**, 15006 (2016)

[13]. M. Jahan, Q. Bao, K. P. Loh, Electrocatallytically active graphene-porphyrin MOF composite for oxygen reduction reaction. *J. Am. Chem. Soc.*, **134**, 6707-6713 (2012).

[14]. M. Jahan, Z. Liu, K. P. Loh, A graphene oxide and copper-centered metal organic framework composite as a tri-functional catalyst for HER, OER, and ORR. *Adv. Funct. Mater.*, **23**, 5363-5372 (2013).

[15] P.T Mosely, A. Cooper. Progress towards an advanced lead-acid battery for use in electric vehicles. J. Power Sources **78,** 244-250 (1999)

[16] I. Hadjipaschalis, A. Poullikkas, Overview of current and future energy storage technologies for electric power applications. *Renewable and sustainable energy reviews* **13**, 1513-1522 (2009)

[17] A. Yoshino, The birth of the lithium ion battery. *Angew. Chem. Int. Ed.* **51**, 5798-5800 (2012)

[18] J. S. Lee, S. T. Kim, R. Cao, N. S. Choi, M. Liu, J. P. Cho, metal air batteries with high energy density: Li-air versus Zn-Air. *Adv. Energy Mater.* **1**, 34-50 (2011)

[19] F. Cheng, J. Chen, Metal-air batteries: from oxygen reduction electrochemistry to cathode catalysts. *Chem. Soc. Rev.* **41**, 2172-2192(2012)

[20] J. Read, Characterization of the lithium/oxygen organic electrolyte battery. *J. Electrochem. Soc.* **149**, A1190- A1195 (2002)

[21] S.B. Saidman, J.B. Bessone, Activation of aluminum by indium ions in chloride solutions. *Electrochim. Acta* **42**, 413-420 (1997)

[22] A. R. Despic, D. M. Drazic, M. M. Purenovic, N. Cikovic, Electrochemical properties of aluminum alloys containing indium, gallium and thallium. *J. Appl. Electrochem.* **6**, 527-542 (1976)

[23] H.A. El Shayeb, F.M. Abd El Wahab, S. Zein El Abedin, Electrochemical behavior of Al, Al-Sn, Al-Zn and Al-Zn-Sn alloys in chloride solutions containing stannous ions. *Corros. Sci.* **43**, 655-669 (2001)

[24] S.Z. El Abedin, F. Endres, Electrochemical behavior of Al, Al-In and Al-Ga-In alloys in chloride solutions containing zinc ions. *J. Appl. Electrochem.* **34**, 1071-1080(2004)

[25] J. Zhang, Z. Zhao, Z. Xia, L. Dai, A metal free bifunctional electrocatalyst for oxygen reduction and oxygen evolution reactions, *Nat. Nanotech.* **10**, 444-452 (2015)

[26] Y. Li, M. Gong, Y. Liang, J. Feng, J. E. Kim, H. Wang, G. Hong, B. Zhang, H. Dai, Advanced zinc-air batteries based on high-performance hybrid electrocatalysts. *Nat. Comm.* **4**, 1805 (2013)

[27] Z. Chen, A. Yu, D. Higgins, H.Li, H. Wang, Z. Chen, Highly active and durable core-corona structured bifunctional catalyst for rechargeable metal-air battery application. *Nano Lett.* **12**, 1946-1952 (2012)

[28] G. Wu, P. Zelenay, Nanostructured nonprecious metal catalysts for oxygen reduction reaction. *Acc. Chem. Res.* **46**. 1878-1889 (2013)

[29] Q. Li, R. Cao, J. Cho, G. Wu, Nanocarbon electrocatalysts for oxygen reduction in alkaline media for advanced energy conversion and storage. *Adv. Energy Mater.* **4**, 1301415 (2014)

[30] J. Suntivich, H. A. Gasteiger, N. Yabuuchi, H. Nakanishi, J. B. Goodneough, S. H. Yang, Design, principles for oxygen-reduction activity on perovskite oxide catalysts for fuel cells and metal-air batteries. *Nat. Chem.* **3**, 546-550 (2011)

[31] Y. Liang, H. Wang, J. Zhou, Y. Li, J. Wang, T. Regier, H. Dai, Covalent hybrid spinel manganese-cobalt oxide and graphene as advanced oxygen reduction electrocatalysts. *J. Am. Chem. Soc.* **134**, 3517-3523 (2012)

[32] J. Liang, Y. Jiao, M. Jaroniec, S. Z. Qiao, Sulfur and nitrogen dual-doped mesoporous graphene electrocatalyst for oxygen reduction reaction with synergistically enhanced performance. *Angew. Chem. Int. Ed.* **51**, 11496-11500 (2012)

[33] Y. Jiao, Y. Zheng, M. Jaroniec, S. Z. Qiao, Origin of the electrocatalytic oxygen reduction activity of graphene-based catalyst: a road map to achieve the best performance. *J. Am. Chem. Soc.* **136**, 4394-4403 (2014)

[34] Y. Zhao, R. Nakamura, K. Kamiya, S. Nakanishi, K. Hashimoto, Nitrogen-doped carbon nanomaterials as non-metal electrocatalysts for water oxidation. *Nat. Comm.* **4**, 2390 (2013)

[35] W. Yang, T. P. Fellinger, M. Antonietti, Efficient metal-free oxygen reduction in alkaline medium on high-surface-area mesoporous nitrogen-doped carbons made from ionic liquids and nucleobases. *J. Am. Chem. Soc*. **133**, 206-209 (2011)

[36] K. Gong, F. Du, Z. Xia, M. Durstock L. Dai, Nitrogen-doped carbon nanotube arrays with high electrocatalytic activity for oxygen reduction. *Science* **332**, 443-447 (2009)

[37] L. Jorissen, Bifuctional oxygen/air electrodes. *J. Power Sources* **155**, 23-32 (2006)

[38] J. L. C. Rowsell, O. M. Yaghi, Metal-organic frameworks: a new class of porous materials. *Microporous and Mesoporous Material* **73**, 3-14 (2004)

[39] S. Kitagawa, R. Kitaura, S. Noro, Functional porous coordination polymers. *Angew. Chem. Int. Ed.* **43**, 2334-2375 (2004)

40 J. R. Long, O. M. Yaghi, The pervasive chemistry of metal-organic frameworks. *Chem. Soc. Rev.* **38**, 1213-1214 (2008)

41 H. C. Zhou, J. R. Long, O. M. Yaghi, Introduction to metal-organic frameworks. *Chem. Rev.* **112**, 673-674 (2012)

42 B. F. Hoskins and R. Robson, Design and construction of a new class of scaffolding-like materials comprising infinite polymeric frameworks of 3D-linked molecular rods. A reappraisal of the zinc cyanide and cadmium cyanide structures and the synthesis and structure of the diamond-related frameworks [N(CH3)4][CuIZnII(CN)4] and CuI[4,4',4'',4'''-tetracyanotetraphenylmethane]BF4.xC6H5NO2, *J. Am. Chem. Soc.* **112**, 1546-1554 (1990)

43 A. U. Czaja, N. Trukhan, U. Muller, Industrial applications of metal-organic frameworks *Chem. Soc. Rev.* **38**, 1284-1293 (2009)

44 (*a*) D. Venkataraman, G. B. Gardner, S. Lee and J. S. Moore, Zeolite-like behavior of a coordination network. *J. Am. Chem. Soc.* **117**, 11600 (1995) (*b*) G. B. Gardner, D. Venkataraman, J. S. Moore and S. Lee, spontaneous as *Nature* **374**, 792 (1995)

45 O. M. Yaghi, G. M. Li and H. L. Li, Selective binding and removal of guests in a microporous metal-organic framework. *Nature* **378**, 703(1995)

46 S. Subramanian and M. J. Zaworotko, Porous Solids by Design: [Zn(4,4′-bpy)$_2$(SiF$_6$)]$n·x$DMF, a Single Framework Octahedral Coordination Polymer with Large Square Channels. *Angew. Chem., Int. Ed. Engl.* **34**, 2127 (1995)

47 S. L. James, Metal-organic frameworks. *Chem. Soc. Rev*., 2003, **32**, 276-288 (2003)

48 H. Li, M. Eddaoudi, M. O'Keeffe, O. M. Yaghi, Design and synthesis of an exceptionally stable and highly porous metal-organic framework. *nature*, **402,** 276-279(1999)

49 M. Eddaoudi, H.Li, O. M. Yaghi, Highly porous and stable metal-organic frameworks. *J. Am. Chem. Soc.* **122**, 1391-1397 (2000)

50 M. Eddaoudi, D. B. Moler, H. Li, B. Chen, T. M. Reineke, M. O'Keeffe, O. M. Yaghi, *Acc. Chem. Res.*, 2001, **34**, 319-330

51 A. H. Chughtai, N. Ahmad, H. A. Younus, A. Laypkov, F. Verpoort, Metal-organic frameworks: versatile heterogeous catalysts for efficient catalytic organic transformations. *Chem. Soc. Rev*. **44**, 6804-6849 (2015)

52 D. Farrusseng, S. Aguado, C. Pinel, Metal-organic frameworks: opportunities for catalysis. *Angew. Chem. Int. Ed.* **48**, 7502-7513 (2009)

53 J.-R. Li, R.J. Kuppler, H.-C. Zhou, Selective gas adsorption and separation in metal–organic frameworks *Chem. Soc. Rev.* **38**, 1477–1504 (2009)

54 L.J. Murray, M. Dinca, J.R. Long, Hydrogen storage in metal-organic frameworks. *Chem. Soc. Rev.* **38**, 1294–1314 (2009)

55 J. Sculley, D. Yuan, H.-C. Zhou, The current status of hydrogen storage in metal-organic frameworks-updated. *Energy Environ. Sci.* **4**, 2721–2735 (2011)

56 M. Dinca, J.R. Long, Hydrogen storage in microporous metal-organic frameworks with exposed metal sites. *Angew. Chem. Int. Ed.* **47** 6766–6779 (2008)

57 B. Chen, S. Xiang, G. Qian, Metal-organic frameworks with functional pores for recognition of small

molecules, *Acc. Chem. Res*. **43**, 1115-1124 (2010)

58 R. Díaz, M. G. Orcajo, J. A. Botas, G. Calleja and J. Palma, Co8-MOF-5 as electrode for supercapacitor. *Mater. Lett.*, **68**, 126–128 (2012)

59 X. Wu, W. Deng, J. Qian, Y. Cao, X. Ai and H. Yang, Single-crystal FeFe(CN)$_6$ nanoparticles: a high capacity and high rate cathode for Na-ion batteries. *J. Mater. Chem. A*, **1**, 10130–10134 (2013)

60 L. Yang, S. Kinoshita, T. Yamada, S. Kanda, H. Kitagawa, M. Tokunaga, T. Ishimoto, T. Ogura, R. Nagumo, A. Miyamoto and M. Koyama, A metal-organic framework as an electrocatalyst for ethanol oxidation. *Angew. Chem., Int. Ed.*, **49**, 5348–5351 (2010)

61 G. Férey, F. Millange, M. Morcrette, C. Serre, M.-L. Doublet, J.-M. Grenèche and J.-M. Tarascon, Mixed-valence Li/Fe-based metal-organic frameworks with both reversible redox and sorption properties. *Angew. Chem., Int. Ed.* **46**, 3259–3263 (2007)

62 C. Combelles, M. B. Yahia, L. Pedesseau and M. L. Doublet, Design of electrode materials for lithium-ion batteries: the example of metal-organic frameworks. *J. Phys. Chem. C*, **114**, 9518–9527 (2010)

63 W. Xia, A. Mahmood, R. Zou, Q. Xu, Metal-organic frameworks and their derived nanostructures for electrochemical energy storage and conversion. *Energy Environ. Sci.* **8**, 1837-1866 (2015)

64 K. Saravanan, M. Nagarathinam, P. Balaya and J. J. Vittal, Lithium storage in a metal organic framework with diamondoid topology- a case study on metal formats. *J. Mater. Chem.*, **20**, 8329–8335 (2010)

65 G. D. Combarieu, S. Hamelet, F. Millange, M. Morcrette, J.-M. Tarascon, G. Férey and R. I. Walton, *In situ* Fe XAFS of reversible lithium insertion in a flexible metal organic framework material. *Electrochem. Commun.* **11**, 1881–1884 (2009)

66 C. Combelles, M. Ben Yahia, L. Pedesseau and M. L. Doublet, Fe^{II}/Fe^{III} mixed-valence state induced by Li-insertion into the metal-organic framework Mil53(Fe): A DFT-U study. *J. Power Sources* **196**, 3426–3432 (2011)

67 M. Okubo, C. H. Li and D. R. Talham, High rate sodium ion insertion into core-shell nanoparticles of Prussian blue analogues. *Chem. Commun.*, **50**, 1353–1355 (2014)

68 Y. Yue, A. J. Binder, B. Guo, Z. Zhang, Z. A. Qiao, C. Tian and S. Dai, Mesoporous Prussian blue analogue: template-free synthesis and sodium-ion battery application. *Angew. Chem. Int. Ed.* **53**, 3134–3137 (2014)

69 F. Meng, Z. Fang, Z. Li, W. Xu, M. Wang, Y. Liu, J. Zhang, W. Wang, D. Zhao and X. Guo, Porous Co$_3$O$_4$ materials prepared by solid-state thermolysis of a novel Co-MOF crystal and their superior energy storage performance for supercapacitor. *J. Mater. Chem. A*, **1**, 7235–7241 (2013)

70 A. Aijaz, N. Fujiwara and Q. Xu, From metal-organic framework to nitrogen-decorated nanoporous carbon: high CO$_2$ uptake and efficient catalytic oxygen reduction. *J. Am. Chem. Soc.*, **136**, 6790–6793 (2014)

71 B. Y. Xia, Y. Yan, N. Li, H. B. Wu, X. W. Lou, X. Wang, A metal-organic frameworks-derived bifunctional oxygen electrocatalysts. *Nat. Energy,* **1**, (2016)

72 J. R. Akridge, Y. V. Mikhaylik and N. White, Li/S fundamental chemistry and application to high performance rechargeable batteries. *Solid State Ionics*, **175**, 243–245 (2004)

73 S. Bai, X. Lui, K. Zhu, S. Wu, H. Zhou, Metal-organic framework-based separator for lithium-sulfur for batteries. *Nat. Energy,* **1**, (2016)

[74] M. L. Aubrey, J. R. Long. A dual-ion battery cathode via oxidative insertion of anions in a metal-organic framework. *J. Am. Chem. Soc.* **137**, 13594-13602 (2015)

[75] M. Inukai, S. Horike, R. Itakura, R. Kiyanagi, S. Kitagawa, Encapsulation mobile proton carriers into structural defects in coordination polymer crystals: high anhydrous proton conduction and fuel cell application, *J. Am. Chem. Soc.* **138**, 8505-8511 (2016)

[76]. R. A. Smaldone, R. S. Forgan, H. Furukawa, J. J. Gassensmith, A. M. Z. Slawin, O. M. Yaghi, J. F. Stoddart, Metal-organic frameworks from edible natural products. *Angew. Chem. Int. Ed.* **49**, 8630-8634 (2010).

[77]. Y. Wei, S. Han, D. A. Walker, P. E. Fuller, B. A. Grzybowski, Nanoparticle core/shell architectures within MOF crystal synthesized by reaction diffusion. *Angew. Chem. Int. Ed.* **51**, 7435-7439 (2012).

[78]. S. M. Yoon, S. C. Warren, B. A. Grzybowski, Storage of electrical information in metal-organic-framework memristors. *Angew. Chem. Int. Ed*. **53**, 4437-4441 (2014)

[79]. S. S. Nagarkar, *et al*. High hydroxide conductivity in a chemically stable crystalline metal-organic framework containing a water-hydroxide supramolecular chain. *Chem. Commun.* **52**, 8459-8462 (2016)

[80]. C. Montoro, P. Ocón, F. Zamora, J. A. R. Navaro, Metal-organic frameworks containing missing – linker defect leading to high hydroxide-ion conductivity. *Chem. Eur. J.* **22**, 1646-1651 (2016).

[81]. M. Sadakiyo, H. Kasai, K. Kato, M. Takata, M. yamauchi, *J. Am. Chem.Soc.*, Design and synthesis of hydroxide ion-conductive metal-organic frameworks based on salt inclusion. **136,** 1702-1705 (2014).

[82]. S.M. Yoon *et al.* High and highly anisotropic proton conductivity in organic molecular porous materials. *Angew. Chem. Int. Ed*. **50**, 7870-7873 (2011)

[83]. J. J. Gassensmith, J. Y. Kim, J. M. Holcroft, O. K. Farha, J. F. Stoddart, J. T. Hupp, N. C. Jeong, A metal-organic framework-based material for electrochemical sensing of carbon dioxide. *J. Am. Chem. Soc.,* **136**, 8277-8282 (2014).

[84]. S. Zaromb, The use and behavior of aluminum anodes in alkaline primary batteries. *J. Electrochem. Soc.* **109**, 1125-1130 (1962)

[85]. Y. Xue, T. Xu, R. Fu, Y. Cheng, W. Yang, Catalytic water dissociation using hyperbranched aliphatic polyester (Boltorn® series) as the interface of a bipolar membrane *J. Colloid Inter. Sci*. **316**, 604-611 (2007)

[86]. E. M. Sherif, S. M. Park, Effects of 1,4-naphthoquinone on aluminum corrosion in 0.5M sodium chloride solutions. *Electro. Acta* **51**, 1313-1321 (2006)

[87]. S. Khireche, D. Boughrara, A. Kadri, L. Hamadou, N. Benbrahim, Corrosion mechanism of Al, Al-Zn and Al-Zn-Sn alloys in 3 wt. % NaCl. *Corrosion Sci*. **87**, 504-516 (2014)

[88]. P. E. Morris and R. C. Scarberry, Predicting corrosion rates with the potentiostat. *Corrosion*, **28**, 444-452 (1972).

[89]. Y. Li, *et al*. Advanced zinc-air batteries based on high-performance hybrid electrocatalysts. *Nat. Comm.* **4**, 1805 (2013)

[90]. Z. Chen *et al*. Highly active and durable core–corona structured bifunctional catalyst for rechargeable metal–air battery application. *Nano Lett*. **12**, 1946-1952 (2012)

[92]. A. S. Arico, S. Srinivasan, V. Antonucci, DMFCs: from fundamental aspects to technology development. *Fuel Cells,* **1**, 133–161 (2001).

93. A. Chen, P. Holt-Hindle, Platinum-based nanostructured materials: synthesis, properties, and applications. *Chem. Rev.* **110**, 3767–3804 (2010).

94. M. Jahan, Q. Bao, K. P. Loh, Electrocatallytically active graphene-porphyrin MOF composite for oxygen reduction reaction. *J. Am. Chem. Soc.*, **134**, 6707-6713 (2012).

95. M. Jahan, Z. Liu, K. P. Loh, A graphene oxide and copper-centered metal organic framework composite as a tri-functional catalyst for HER, OER, and ORR. *Adv. Funct. Mater.*, **23**, 5363-5372 (2013).

96. R. Liu, D. Wu, X. Feng, K. Müllen, Nitrogen-doped ordered mesoporous graphitic arrays with high electrocatalytic activity for oxygen reduction, *Angew. Chem. Int. Ed.*, **49**, 2565-2569 (2010)

97. J. J. Gassensmith, *et al.* Strong and reversible binding of carbon dioxide in a green metal-organic framework. *J. Am. Chem. Soc.* **133**,15312-15315 (2011)

98. I. M. Aldous, L. J. Hardwick, Solvent-mediated control of the electrochemical discharge products of non-aqueous sodium-oxygen electrochemistry. *Angew. Chem. Int. Ed.* **55**, 8254-8257 (2016)

99. N. Fujiwara, *et al.* Reversible air electrodes integrated with an anion-exchange membrane for secondary air batteries *J. Power Sources* **196**, 808-813 (2011)

100. R. M. A. Tehrani, S. A. Ghani, The nanocrystalline nickel with catalytic properties on methanol oxidation in alkaline medium. Fuel Cells **9**, 579-587. **(2009)**

101. L. Jörissen, Bifunctional oxygen/air electrodes. *J. Power Sources* **155**, 23-32 (2006)

102. P. Xie, M. Z. Rong, M. Q. Zhang, Moisture battery formed by direct contact of magnesium with foamed polyaniline. *Angew. Chem. Int. Ed.* **55**, 1805-1809 (2016)

103. B. Dholakiya. Ch.7 in *Unsaturated polyester resin for specialty applications*. INTECH (2012)

104. S. Ibrahim, Esterification reaction for novel synthesis castor-based polyester and formulation as base oil in synthetic drilling fluid. *Inter. J. Sci. Res.* **3**, 1969-1975 (2014)

105. C. G. Morales-Guio, L. A. Stern, X. Hu, Nanostructured hydrotreating catalysts for electrochemical hydrogen evolution. *Chem. Soc. Rev.* **43**, 6555-6569 (2014)

106. S. M. Yoon, J. H. Park, B. A. Grzybowski, Large-area, freestanding MOF films of planar, curvilinear or micropatterned topographies. Angew. Chem. Int. Ed. (2016)

107. G. Göransson, E. Ahlberg, Oxygen reduction in alkaline solution using mixed carbon paste/NixCo1-xO electrodes. *Electrochem. Acta* **146**, 638-645 (2014)

108. R. A. Smaldone, R. S. Forgan, H. Furukawa, J. J. Gassensmith, A. M. Z. Slawin, O. M. Yaghi, J. F. Stoddart, Metal-organic frameworks from edible natural products. *Angew. Chem. Int. Ed.* **49**, 8630-8634 (2010).

109. Y. Wei, S. Han, D. A. Walker, P. E. Fuller, B. A. Grzybowski, Nanoparticle core/shell architectures within mof crystal synthesized by reaction diffusion. *Angew. Chem. Int. Ed.* **51**, 7435-7439 (2012).

110. A. S. Liu, M. A. S. Oliveira, Electrodeposition of polypyrrole films on aluminum from tartrate aqueous solution. *J. Brazilian Chem. Soc.* **18**, 143-152 (2007).

Acknowledgement

First of all, I would like to express appreciation to my committees, my advisor, Professor Bartosz A. Grzybowski, for his guidance during my master course. I remember his asking, "Do you want to become a scientist?" which was heavy question to me but, it made me overcome adversity. He expertly taught me through giving passion of science and great education. I impressed his love for science that made me keep mind of exploring research.

Also, my appreciation expends to Dr. Seokmin Yoon. He always told me "take care of your research and consider your experiment as your baby" By his advices, I realized that my insight was quite narrow and I was thinking only small things. His mentoring and encouragement change my values. Thanks to professor KwangS Kim for being my committee and viewing favorably my project.

I thanks to my group members, especially, Dr. Yong-Kwang Jeong, Dr. Slawek Lach, Jun Heuk Park. I haven't solved my project without their helps and encouraging. I would like to appreciate to professor Jin-Kyun Park, without his advice and suggestion of direction, I would never have been got opportunity of research here. And I thanks to my friends, JeongSun Park, TaeSeung Yoon, YuRan Jo, Jin-A Nam, SaeBom Kim, MeeJin Yu, MyungWon Song, Gibeom Nam and CheolHyun Kim for helping and inspiring me endure hardship.

Finally, Thanks to my grandmother, mother, father and my brother SangHyun Cho for cheering and praying me at all times. I would like to appreciate all one more.